The root to the Galápagos mantle plume on the core-mantle boundary

Sanne Cottaar[1]*, Carl Martin[1], Zhi Li[1], Rita Parai[2]

1. Department of Earth Sciences, University of Cambridge, Cambridge, UK
2. Department of Earth and Planetary Sciences, Washington University in St Louis, St Louis, MO, USA

* corresponding author: sc845@cam.ac.uk

The root to the Galápagos mantle plume on the core-mantle boundary

Sanne Cottaar[1]*, Carl Martin[1], Zhi Li[1], Rita Parai[2]

3. Department of Earth Sciences, University of Cambridge, Cambridge, UK
4. Department of Earth and Planetary Sciences, Washington University in St Louis, St Louis, MO, USA

* corresponding author: sc845@cam.ac.uk

Author ORCIDs

A. Sanne Cottaar: 0000-0003-0493-6570
B. Carl Martin: 0000-0002-2882-543X
C. Zhi Li: 0000-0001-5657-655X
D. Rita Parai: 0000-0002-9754-7349

Author contributions

Conceptualization: A. SC
Methodology: A. SC, B. CM, C. ZL
Investigation: A. SC, B. CM, D. RP
Visualization: A. SC, B. CM
Writing—original draft: A. SC, D. RP
Writing—review & editing: A. SC, B. CM, C. ZL, D. RP

Abstract

Ultra-low velocity zones (ULVZs) are thin anomalous patches on the boundary between the Earth's core and mantle, revealed by their effects on the seismic waves that propagate through them. Here we map a broad ULVZ near the Galápagos hotspot using shear-diffracted waves. Forward modelling assuming a cylindrical shape shows the patch is ~600 km wide, ~20 km high, and its shear velocities are ~25% reduced. The ULVZ is comparable to other broad ULVZs mapped on the core-mantle boundary near Hawaii, Iceland, and Samoa. Strikingly, all four hotspots where the mantle plume appears rooted by these 'mega-ULVZs', show similar anomalous isotopic signatures in He, Ne, and W in their ocean island basalts. This correlation suggests mega-ULVZs might be primordial or caused by interaction with the core, and some material from ULVZs is entrained within the plume. For the Galápagos, the connection implies the plume is offset to the west towards the base of the mantle.

Non-technical summary

Observations of deep-diving earthquake waves reveal heterogeneity and dynamics within the Earth. Here we use waves that diffract along the boundary between the core and the mantle to map a patch of anomalous material on top of the boundary. The waves propagating within the patch are slowed down by 25% compared to those propagating in surrounding material, and the waves are refracted when entering and exiting the patch. These waves arrive at seismic stations delayed by tens of seconds. By modelling the waveforms, and mapping the directionality of this delayed energy, we constrain the location of the patch beneath the eastern Pacific and to the west of the Galápagos archipelago. The patch can be approximated

as a cylinder with a width of 600 km and height of 20 km. Such patches are named ultra-low velocity zones or ULVZs. Similar large ULVZs are found near other intraplate volcanic hotspots, i.e. Hawaii, Iceland and Samoa. Volcanic basalts on these islands and the Galápagos show anomalous isotopic signatures, which could be dragged up in a mantle plume from the ULVZ at the core-mantle boundary and indicate that the material within the ULVZs was either created early in Earth's history or contains material leaking from the core.

1. Introduction

The lowermost hundreds of kilometers of the mantle are the lower thermal boundary layer in mantle dynamics, which is partially driven by heat flow across the core-mantle boundary. The layer plays a major role in Earth's thermal and dynamical history. Seismic waves have revealed it is characterized by strong lateral variations in seismic wave speed, which are linked to variations in temperature and composition. On the global scale, there are two widespread regions with relatively slow seismic velocities, dubbed Large Low Velocity Provinces (LLVPs, e.g. Cottaar and Lekić, 2016; Garnero *et al.*, 2016), which are surrounded by regions of relatively fast seismic velocities that can be interpreted as the accumulation of subducted tectonic plates or slabs, e.g. (Van der Hilst, Widiyantoro and Engdahl, 1997; Domeier *et al.*, 2016). Much thinner in nature, on the order of 10s of km, but more extreme in their velocity anomaly, are the ultra-low velocity zones (ULVZs). ULVZs appear patchy in nature and are directly on the core-mantle boundary. While only a fraction of the core-mantle boundary has been targeted for these anomalies, there is a weak trend that these patches appear within or near the LLVPs (Yu and Garnero, 2018). This relationship is however certainly true for the broadest of ULVZs that have been mapped in 3D (Cottaar and Romanowicz, 2012; Thorne *et al.*, 2013; Yuan and Romanowicz, 2017; Jenkins *et al.*, 2021; Lai *et al.*, 2022; Li *et al.*, 2022; Li, Sun and Bower, 2022), and can be dubbed 'mega-ULVZs' after Thorne *et al.* (2013).The three mega-ULVZs currently mapped lie in the vicinity of the Hawaiian, Icelandic and Samoan hotspots, and such large structures appear otherwise rare, at least across a large swath of the Pacific (Kim *et al.*, 2020).

The nature and origin of ULVZs are uncertain. Their velocity reductions are so extreme that their composition must be anomalous, and enrichment of magnesiowüstites is a prime candidate (Wicks *et al.*, 2017; Dobrosavljevic, Sturhahn and Jackson, 2019). The presence of partial melt is also proposed, but is unlikely to form stable ULVZs (Hernlund and Jellinek, 2010; Dannberg *et al.*, 2021). Solid-state ULVZs could be remnants of an early molten mantle, becoming enriched in magnesiowüstite due to fractional crystallization, and therefore have a primordial origin (Labrosse, Hernlund and Coltice, 2007). The potential of Fe-enrichment by the core has also been proposed, through mechanisms of diffusion (Hayden and Watson, 2007; Lesher *et al.*, 2020) or mechanisms driven by morphological instabilities (Kanda and Stevenson, 2006; Otsuka and Karato, 2012; Lim, Bonati and Hernlund, 2021). If ULVZs are dense in composition, questions remain as to whether they are passive markers of surrounding convection (Li *et al.*,

2017; Li, Sun and Bower, 2022), play an active role by rooting mantle plumes (Jellinek and Manga, 2004), and if their material can be entrained in plumes (Jones, Davies and Sossi, 2019).

Here we present evidence for the presence of a mega-ULVZ on the core-mantle boundary to the west of the Galápagos hotspot using shear diffracted waves. Shear diffracted energy incident upon a mega-ULVZ, causes guided waves within. This energy is refracted due to the velocity contrast at the entry to and exit from the ULVZ. At a seismic station, the refracted energy arrives off-angle and delayed by 10s of seconds. We refer to this as the 'Sdiff postcursor'. The frequency content of the postcursors is sensitive to the height of the ULVZ. Their delay times are sensitive to the size, shape, and velocity reduction of the ULVZ. We focus on four earthquakes with Sdiff postcursors sampling the core-mantle boundary near the Galápagos. Our preferred ULVZ model is found by synthetic waveform modelling for 3D ULVZ models, and by imaging the directionality of the postcursor energy.

2. Data and Methods

2.1 Data Catalogue

Recognizing consistent arrivals of Sdiff postcursors caused by a mega-ULVZ requires dense data coverage. The Transportable Array (TA) is a large-scale deployment of 400 seismic stations that has gradually moved from west to east across the conterminous United States between 2004 and 2015 with a rough station spacing of 70 km. The presence of the TA here played a major role in the discovery and mapping of the Hawaiian, Samoan and Icelandic mega-ULVZs (Cottaar and Romanowicz, 2012; Thorne *et al.*, 2013; Yuan and Romanowicz, 2017). Over several years since 2014, the TA was transferred to Alaska, monitoring the most seismically active state of the US with unprecedented coverage, while also providing new geometries to study the core-mantle boundary. Observations of Sdiff waves from Chilean earthquakes to the Alaska TA provided us with the first evidence of the presence of Sdiff postcursors caused by a ULVZ beneath the eastern Pacific. Subsequently, we built a catalogue of postcursor observations.

We visually assess earthquake data for the presence of Sdiff postcursors caused by a ULVZ near the Galápagos from a globally compiled data set of Sdiff phases for all earthquakes over a magnitude of 5.7 and for all depth ranges. Data are filtered between 10 and 30 s. To assess, Sdiff phases are aligned on their predicted arrival time and organized as a function of azimuth. A postcursor is recognized by strong later arrival that has a move-out in time as a function of azimuth with respect to the main Sdiff arrival. They can only be observed if there is sufficient data coverage, a good signal-to-noise ratio, and no strong interfering depth phases. A catalogue of promising observations of postcursors caused by the Galápagos ULVZ is given in Table S1. We focus on four high quality events that observe the Galápagos ULVZ from a variety of angles. For these events, we quality check the data by eye, and remove traces with low signal-to-noise

ratio. Several further examples of postcursor observations are presented in the supplementary materials.

2.2 Forward modelling

We compute full waveform synthetics for 3D ULVZ models using the "sandwiched" version of the Coupled Spectral Element Method (sandwiched-CSEM, Capdeville *et al.*, 2002, 2003), similar to Cottaar and Romanowicz (2012) and Yuan and Romanowicz (2017). The "sandwiched"-CSEM computes the spectral element solution for a full 3D model in the lowermost 370 km of the mantle, and couples this to a normal mode summation for a 1D model in the rest of the mantle and the core. This method allows for relative computational efficiency to compute synthetics down to periods of 10 seconds for a finely meshed model in the lowermost mantle, at the cost of not having a fully 3D model in the rest of the planet. The internal SEM mesh is defined to have a boundary at the top of the ULVZ.

To reduce the parameter space to search, we assume a cylindrical anomaly for which we determine the radius, height, shear wave velocity reduction, and location in latitude and longitude. Computing full-waveform synthetics is too computationally expensive to allow for a full grid search of all five parameters. Instead, we evaluate the delays, move-outs and amplitudes of resulting postcursors by eye, and adjust the model to approach a better fit.

In the background, we use the radially anisotropic shear velocities of SEMUCB-WM1 (French et al. 2014), and a scaled P-wave model. Both models are tapered to the background 1D model in the top 70 km of the SEM mesh. Inside the ULVZ, the isotropic shear wave velocities are reduced. The Vp reduction is scaled by a factor of 1, but this choice has negligible effect on the Sdiff waveforms. The density deviation is scaled by a factor of -0.5, and is thus increased within the ULVZ, but again has little effect on the Sdiff waveforms.

2.3 Beamforming

Using arrays of seismic stations, we can determine the directionality of incoming energy. Searching over the incoming backazimuth is called beamforming, while searching over the slowness or incident angle is called slant-stacking (or vespa processing, e.g. Rost and Thomas, 2002). Shear diffracted waves have a predicted slowness of 8.32 s/dg for PREM (Dziewonski and Anderson, 1981), but this could vary due to the velocities in the lowermost mantle at the location where the energy propagates upwards to the seismic array. The slowness, or incident angle, could vary slightly between the main wave and the postcursor when they come from different directions. For these reasons, we do not fix the slowness when beamforming, but search over coherent energy by stacking the signals, $s_j(t)$, as a function of time t, slowness, u_{hor}, and backazimuth, θ, for a given subarray,

$$S(t, u_{hor}, \theta) = \sum_{j=1}^{N} s_j(t - \boldsymbol{u_{hor}}(\theta) \cdot \boldsymbol{x_j}), \quad (1)$$

where $\boldsymbol{u_{hor}}(\theta) = u_{hor} \begin{pmatrix} \sin\theta \\ \cos\theta \end{pmatrix} = \begin{pmatrix} u_{EW} \\ u_{NS} \end{pmatrix}$ is the horizontal slowness vector, and $\boldsymbol{x_j} = \begin{pmatrix} x_{EW} \\ x_{NS} \end{pmatrix}_j$ is the distance vector to the centre of the subarray.

A seismic signal can be expressed in amplitude and instantaneous phase:

$$s_j(t) = A_j(t) \exp[i\Phi_j(t)] \quad (2)$$

We create two separate stacks, one stack for the amplitude envelope, S_A, setting $s_j(t) = A_j(t)$, and one stack over the phase, S_Φ ,setting $s_j(t) = \exp[i\Phi_j(t)]$. Finally, we interpret a phase weighted envelope stack (Schimmel and Paulssen, 1997), where the phase is weighted by a factor of 4,

$$PWES = S_A \, {S_\Phi}^4, \quad (3)$$

where all stacks are 3D arrays as a function of (t, u_{hor}, θ).

A light Gaussian filter is applied to the stack to reduce irregularities and allow automated picking of peaks. The main peak and other peaks above 10% of the maximum peak are picked. Uncertainty is established by taking the minimum and maximum values for the contour at 95% of the peak amplitude. An example of a high-quality stack is shown in Fig. S13.

To build subarrays for an event, we create a sliding window in distance-azimuth space. The window is both 5º in distance and in azimuth, and we shift the window every 2º in azimuth and distance. For each window that has at least 12 stations, a stack is considered. The stacks are manually quality controlled for having one or two clear peaks that are well constrained in time-slowness-backazimuth space.

200

Results

2.1 Sdiff postcursor data set

Our analyses are based on waveform data from four different earthquakes (Fig. 1, Table 1). We
205 use shear-diffracted waves recorded at the Alaska TA from two major earthquakes in Chile that sample the core-mantle boundary beneath the Eastern Pacific (Events A and B). Events A and B are shallow thrust event along the Chilean subduction zone of magnitude 7.6 on the 25th of December 2016, and magnitude 6.7 on the 29th of September 2019, respectively.

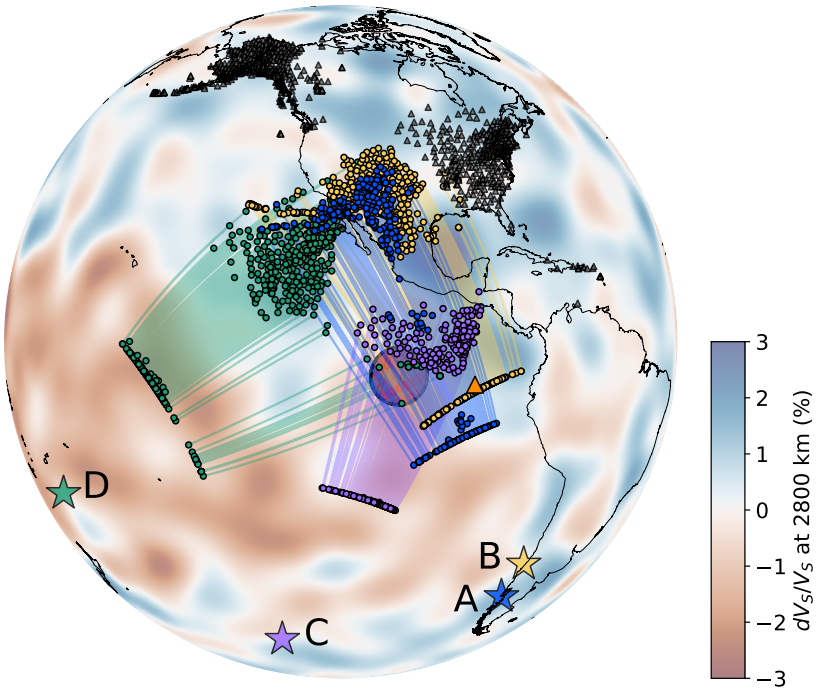

210

Figure 1 Map shows the geometry of the shear diffracted waves. Data geometries are shown by earthquake location (star), station locations (grey triangles), and ray path sensitivity to the core-mantle boundary (shaded regions between piercing points at 2800 km depth).
215 Earthquake locations and ray paths are colored per event: A- blue, B-yellow, C-purple, and D-green. For earthquake parameters, see Table 1. The Galápagos hotspot is indicated by an orange triangle. The location of the Galápagos ULVZ, as constrained in this study, is shown as the red-filled circle. Background model is showing the shear wave velocity deviations at 2800 km depth from the tomographic SEMUCB-WM1 (French and
220 Romanowicz, 2014).

Table 1 Parameters for the earthquakes. All earthquake parameters are from the Global Centroid-Moment Tensor project (Ekström *et al.*, 2012) except for event A, for which the W-phase solution published by the USGS National Earthquake Information Centre provided a better waveform fit. See Table S1 for full catalogue.

	Date	Depth [km]	Lat. [°N]	Long.[° W]	Mw	Location
A	2016/12/25	21.5	-43.41	-73.94	7.6	Southern Chile
B	2019/09/29	16.7	-35.56	-73.10	6.7	Off Coast of Central Chile
C	2015/05/19	14.9	-54.53	-132.39	6.6	Pacific-Antarctic Ridge
D	2017/02/24	417.9	-23.44	-178.77	7.0	South of Fiji Islands

With Sdiff observations from only one azimuthal direction, the location of the ULVZ in the direction of their propagation remains non-unique. To fully constrain the location of ULVZs, we need rays crossing at a different angle. This is provided by Event C, which is a Mw 7.2 on the Pacific-Antarctic ridge, recorded in the north-eastern US and south-eastern Canada. Additional evidence from a third angle comes from recordings across the Caribbean for an event in Fiji, although coverage in this direction is poor (Event D).

Figs. 2-5 show the expected and observed data for events A-D. The SH component of the shear diffracted wave and its postcursor attenuates less along the core-mantle boundary and therefore these phases are best observed on the transverse component. Transverse components shown are bandpass filtered between periods of 10 and 30s. Data are organized as a function of azimuthal angle from the earthquake and windowed around the predicted arrivals times of Sdiff for 1D radial Earth model (PREM, Dziewonski and Anderson, 1981). Expected waveforms are computed synthetics for this 1D radial Earth model showing waveform variations predicted due to source effects, but little waveform complexities, due to the absence of any mantle heterogeneity in the model.

Event A (Fig. 2) is a shallow event, causing the depth phases (pSdiff and sSdiff) to arrive shortly after the main phase. The observed compared to the expected waveforms show evidence for deep 3D heterogeneity in two ways. Firstly, the initial Sdiff phases arrive later at smaller azimuths and earlier at larger azimuths. This variation in travel time is caused by the dichotomy in the

lowermost mantle where the waves at smaller azimuths propagate through the LLVP beneath the Pacific, and the waves at larger azimuths propagate through broad areas of likely subducted slab material (Fig. 1). Secondly, and this is the focus of this study, delayed and significant postcursors are present. The postcursors interfere with the main arrivals at azimuths of 321-327º and move out in time towards larger azimuths. The nature of these postcursors is comparable to those observed for the Hawaiian and Icelandic mega-ULVZs (Cottaar and Romanowicz, 2012; Yuan and Romanowicz, 2017).

Event B (Fig. 3) shows comparable observations to event A. Again, the main Sdiff arrival shows a trend in arrival time with azimuth related to the LLVP boundary, and there is the presence of a postcursor that moves-out towards larger azimuth with respect to the main Sdiff phases. However, the postcursor for this event is much weaker in amplitude relative to the main phase.

Event C (Fig. 4) shows postcursors with a very different propagation path through the same area at the core-mantle boundary. Its postcursors are stronger in amplitude towards larger azimuths and display a weaker move-out with time.

Event D (Fig. 5) shows hints of postcursor energy after the main phase at azimuths above 75º. Due to the poor station coverage in this area though, it is hard to observe any trends in the postcursor behavior. Potentially this data is also affected by a mega-ULVZ beneath the Marquesas as suggested by (Kim *et al.*, 2020), implying there could be two postcursors. The data imaged by stations in the US at smaller azimuths show diffracted waves with no discernible postcursors, suggesting there are no mega-ULVZs located in a broad region of the core-mantle boundary between Hawaii and Marquesas.

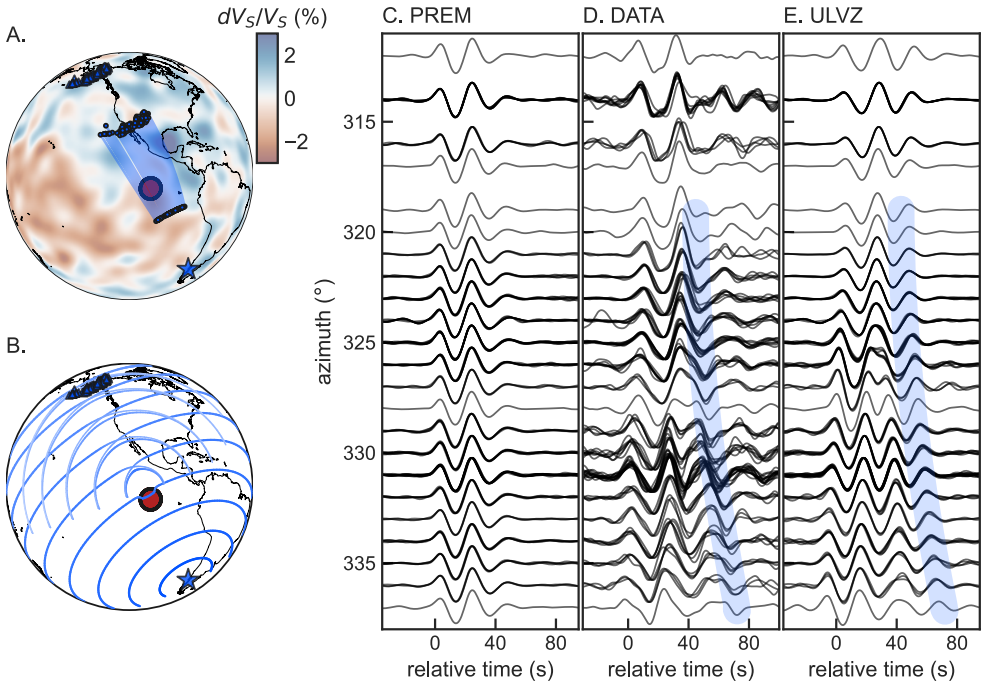

Figure 2 Geometry, data, and synthetics for event A. **(A)** Geometry of data coverage, event (star), stations (triangles), and sensitivity to the core-mantle boundary (shaded region) and ULVZ model (red circle). Background shows the shear wave velocity deviations at 2800 km depth from the tomographic SEMUCB-WM1 (French and Romanowicz, 2014). **(B)** Wavefront predictions for modelled ULVZ illustrating the cause of the postcursors. For an animation, see Movie S1. **(C)** Synthetic waveforms for 1D Earth model PREM (Dziewonski and Anderson, 1981)**(D)** Observed data. **(E)** Synthetics including background tomographic model and the preferred cylindrical ULVZ model. Data panels show SHdiff on the transverse component filtered between 10 and 30 s, binned by azimuth and centered on the predicted arrival times. Postcursor energy is highlighted by shaded region.

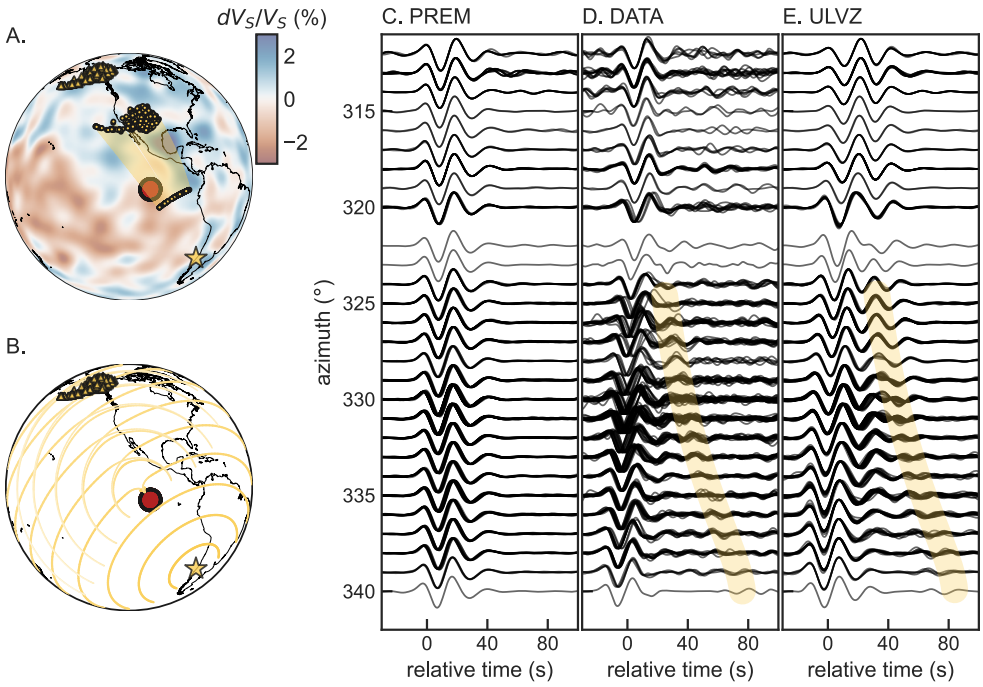

Figure 3. Geometry, data, and synthetics for event B. Same as Figure 2, but for Event B. For an animation, see Movie S2.

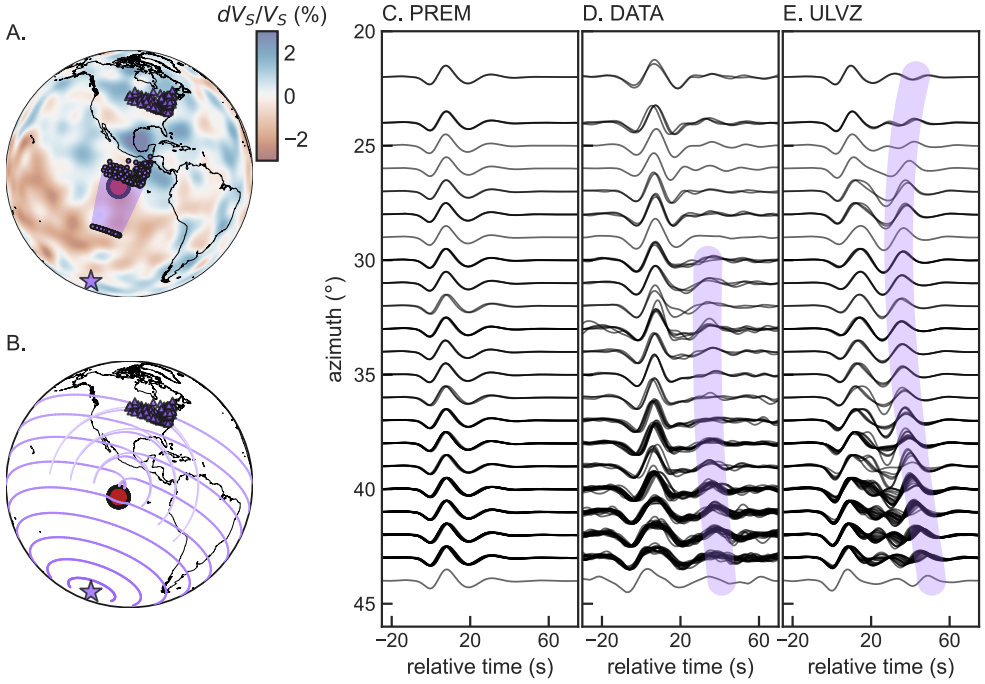

Figure 4. Geometry, data, and synthetics for event C. Same as Figure 2, but for Event C. For an animation, see Movie S3.

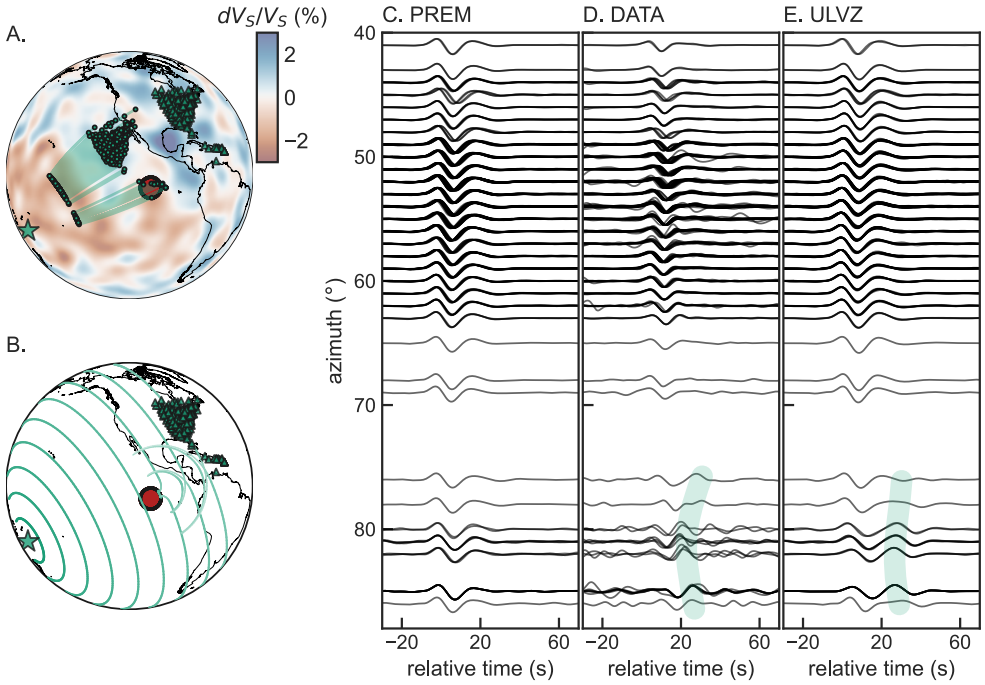

Figure 5. Geometry, data, and synthetics for event D. Same as Figure 2, but for Event D. For an animation, see Movie S4.

2.2 Preferred model

Our best fitting ULVZ is centered at 105º W and 2º N. It has a height of 20 km and a width of 600 km, which is equal to nearly 10º on the core-mantle boundary. The shear wave velocity within is reduced by 25% compared to surroundings. In Figs. 2-5, subplot B shows the wavefront predictions for this ULVZ model computed using a modified version of the wavefront tracker by (Hauser, Sambridge and Rawlinson, 2008). Subplots E show the synthetic waveforms for the preferred ULVZ model. This reproduces the general move-out of the postcursors for Events A-C. It shows the relatively small amplitude postcursor for event B in comparison to event A, which is caused by the earthquake source of event B emitting relatively less shear energy in the direction of the ULVZ. For event C, the weaker move-out of the postcursor with time is predicted. For this event, the synthetics show clear and strong postcursors at smaller azimuths, which is not observed in the data. This could either mean that the assumed source mechanism is poor or that one side of the ULVZ has an irregular boundary or decreases in thickness.

Trade-offs and uncertainties do remain (see Supplementary Materials). Waveform results for shifted and resized ULVZ models are shown in the Figs. S6-S12 to illustrate the sensitivity of the data to various parameters. Uncertainties on the preferred cylindrical model are at least 2º on location, 100 km in width, 5 km in height and 5% in velocity reduction.

2.3 Directionality of postcursors

Our preferred ULVZ model is confirmed by analyzing the directionality of the postcursor waveform by beamforming the energy for subarrays of stations where the main and postcursor are well separated. Fig. 6 shows the results for the significant postcursors present in event A, comparing the results for observations and synthetics. Both data and synthetics show a bimodal distribution of energy peaks, with the later cluster offset by 20-30º in backazimuth. Within error, the offset arrivals originate from the western boundary of the modelled ULVZ. There is an absolute time shift between the data and synthetics, which indicates unmodeled velocity variations along the Sdiff paths, but which are beyond the scope of this study. Beamforming results for other events are discussed in Supplementary Materials and for event C are shown in Fig. S14.

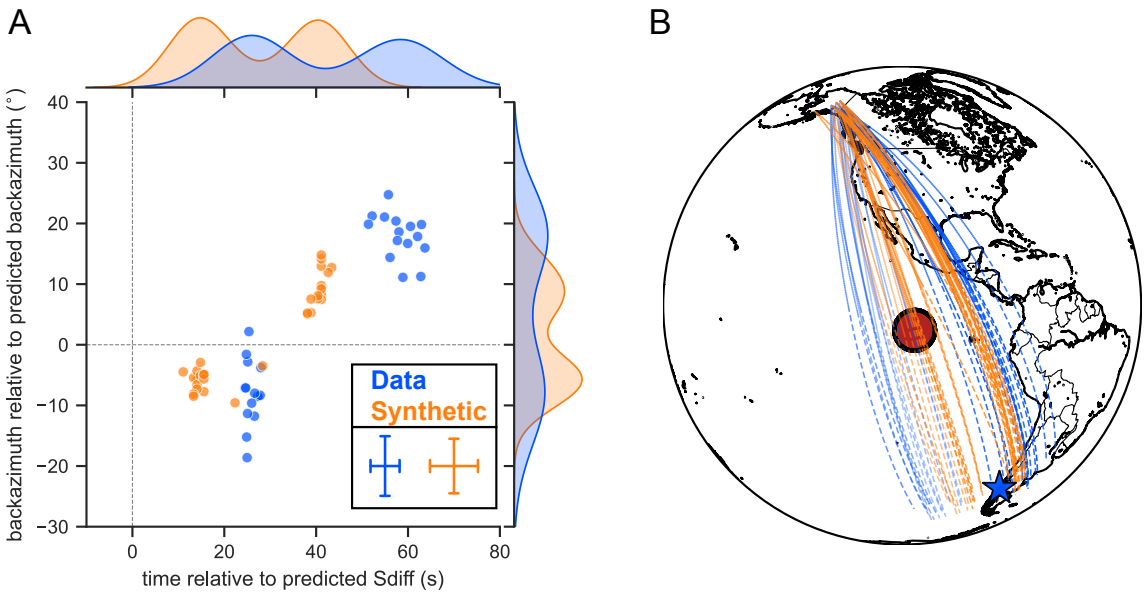

Figure 6 Beamforming results for event A. **(A)** Relative time versus relative backazimuth for picked peaks in beamform stack for real data (blue) and synthetic data for the ULVZ model (orange). Error bars in lower right shows median uncertainty for the observations. Note the bimodal distribution in both time and backazimuth related to the main and postcursor arrival. **(B)** Back-projection of determined backazimuths for energy peaks. Projections are solid line up to 60° epicentral distance and dashed beyond up to 120° epicentral distance. Transparency reflects relative amplitude of the secondary postcursor peaks with respect to the main peaks.

3. Discussion

The Galápagos ULVZ falls into the category of broad-scale mega-ULVZs, which are so far uncovered by diffracted phases. Other occurrences are mapped in 3D near Hawaii (Cottaar and Romanowicz, 2012; Jenkins *et al.*, 2021; Lai *et al.*, 2022; Li, Sun and Bower, 2022; Li *et al.*, 2022), Samoa (Thorne *et al.*, 2013), and Iceland (Yuan and Romanowicz, 2017); these are shown in Fig. 7 combined with the global database of ULVZs by (Yu and Garnero, 2018). In general, a large variation of geometries of ULVZs has been suggested, and it is unclear if these all have comparable compositions and origins, and are shaped due to surrounding flows, or if these are distinctive features formed in different ways. To the south of the Galápagos, for example, ULVZs have been mapped using PKP precursor phases that appear pile or ridge-like with a width of 30 km and a height of 30 km (Ma, Sun and Thomas, 2019), showing a very different aspect ratio from the mega-ULVZ observed here.

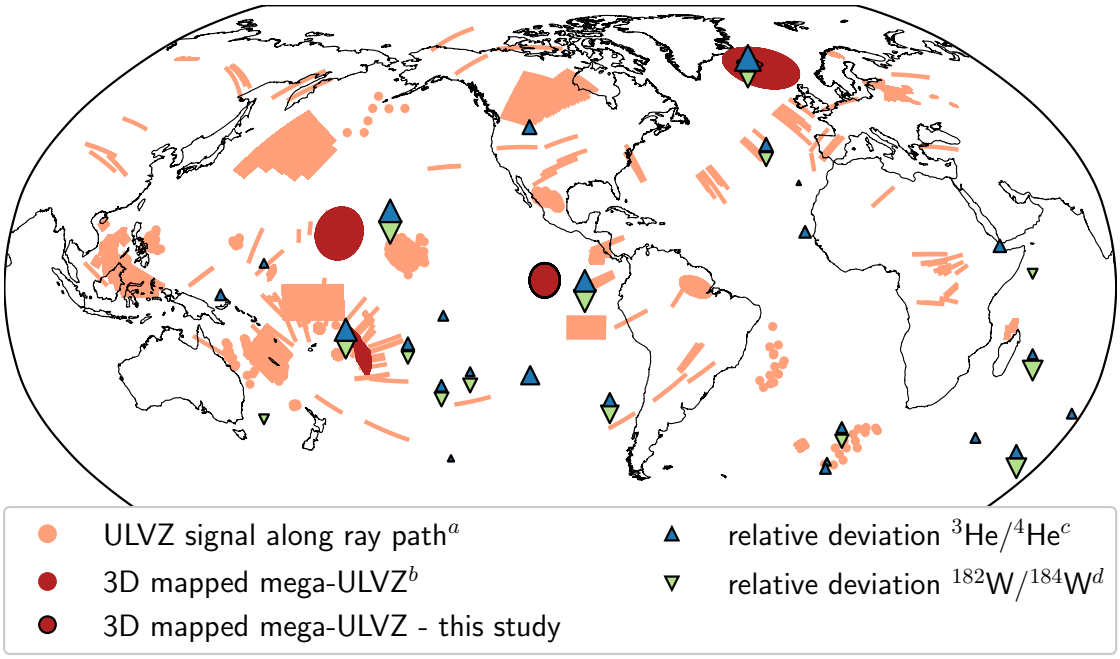

Figure 7. Mapped ULVZs and ocean island basalt isotopic signatures. Previous suggested locations of ULVZs (light orange) and recently 3D mapped mega-ULVZs (red) combined with helium and tungsten isotope ratio deviations observed in ocean island basalts compared to mid-ocean ridge basalts (scaled blue and green triangles, respectively). a. Compilation of ULVZ studies (Yu and Garnero, 2018) and a box is added for the region where small-scaled ridges are found to the south of Galápagos (Ma, Sun and Thomas, 2019), b. Icelandic mega-ULVZ (Yuan and Romanowicz, 2017), Samoan mega-ULVZ (Thorne *et al.*, 2013), Hawaiian mega-ULVZ (Li *et al.*, 2022). c. Scaled maximum observed positive $^{3}He/^{4}He$ isotopic ratio deviations from 9 Ra, the upper end of the MORB range, based on data compiled by (Jackson, Konter and Becker, 2017; Williams *et al.*, 2019); see references therein, and with additions from (Jackson *et al.*, 2020; Peters *et al.*, 2021). d. Largest observed negative deviations in $\mu^{182}W$ compiled from (Mundl *et al.*, 2017; Rizo *et al.*, 2019; Mundl-Petermeier *et al.*, 2020). Note that the largest deviations for He and W do not always occur in the same samples for a given hotspot, and hotspots might be affected to different degrees by overprinting by recycled crust (Parai *et al.*, 2019; Jackson *et al.*, 2020; Péron *et al.*, 2021; Day, Jones and Nicklas, 2022). Additionally, both the compilations of the ULVZs and the isotopic anomalies have a degree of geographical bias to where (more) studies have been conducted.

The edge of our preferred ULVZ location lies ~10º to the west of the Galápagos hotspot. A connection would require the Galápagos mantle plume to be offset in this direction. Seismic tomographic models identify low velocity anomalies beneath the Galápagos, which could be interpreted as plumes, but do not all agree on its direction of tilt or continuity across the mantle. The resolution of the models beneath the Galápagos will be biased due to the seismic stations being largely located on land to the east and north. Some of the latest global mantle shear wave velocity models suggest the plume is offset to the southwest (French and Romanowicz, 2015; Lei

et al., 2020) and this offset also results when combining shear velocity models with a geodynamical model (Williams *et al.*, 2019). A recent innovative use of increasing coverage around the hotspot by using passively floating seismometers resulted in a P wave velocity model with a vertical plume down to 1900 km, beneath which resolution might be lost (Nolet *et al.*, 2019). A different recent P wave velocity model focused on adding coverage in the lower mantle, observes a vertical plume down to 1000 km depth with fast velocities underneath (Hosseini *et al.*, 2020). In both of these P wave models, the suggested plume is vertical. It is however easy to speculate that if there is a whole-mantle plume, that it originates within or at the edge of the LLVP (Steinberger and Torsvik, 2012; Li and Zhong, 2017) and its base is therefore offset to the west or southwest of the hotspot at the surface.

The geochemistry of basalts from the Galápagos archipelago indicate a plume with at least three distinct components, each manifesting in geographically-restricted portions of the archipelago along with a depleted upper mantle component (Geist, White and McBirney, 1988; White, McBirney and Duncan, 1993; Harpp and White, 2001; Gleeson *et al.*, 2021). Harpp and Weis (2020) observed that the plume component mixture evident in the southwestern part of the archipelago is distinct from that in the northeast and argued for a bilaterally asymmetric Galápagos plume. Notably, subaerial and submarine samples from the westernmost island of Fernandina exhibit the highest $^{3}He/^{4}He$ ratios in the archipelago (Graham *et al.*, 1993; Kurz and Geist, 1999; Kurz *et al.*, 2009), and the most solar-like Ne isotopic compositions of ocean islands globally (Kurz *et al.*, 2009; Péron *et al.*, 2021). Solar nebular helium and neon are thought to have dissolved into a terrestrial magma ocean during Earth's accretion (Harper and Jacobsen, 1996). High $^{3}He/^{4}He$ ratios in ocean island basalts (compared to those measured in mid-ocean ridge basalts) reflect greater retention of the primordial helium budget, which mutes the impact of radiogenic ^{4}He ingrowth by decay of U and Th over Earth history (Mukhopadhyay and Parai, 2019; Parai *et al.*, 2019). The Fernandina helium and neon isotopic signatures indicate that the southwestern side of the Galápagos plume samples a reservoir that has experienced relatively little degassing and thus retained a high proportion of primordial solar He and Ne from Earth's accretion.

Four hotspot locations (Hawaii, Iceland, Samoa and Galápagos) that have a mega-ULVZ situated near their projection down onto the core-mantle boundary share a collective set of geochemical features. Samples from these locations exhibit high $^{3}He/^{4}He$ ratios, relatively solar-like Ne isotopes, and anomalous ^{182}W isotopic signatures (Fig. 7). ^{182}W was produced by decay of the extinct radionuclide ^{182}Hf in the first ~60 Myr of Earth history. Core segregation within the lifetime of ^{182}Hf fractionated Hf/W ratios and generated a radiogenic ^{182}W isotopic signature ($\mu^{182}W=0$, where $\mu^{182}W$ signifies the part per million deviation in $^{182}W/^{184}W$ from a laboratory standard) in the bulk silicate Earth compared to chondrites (Kleine *et al.*, 2002; Yin *et al.*, 2002). The core locked in an unradiogenic ^{182}W signature (negative $\mu^{182}W$), as would any other

siderophile-enriched reservoir in the interior that formed during the lifetime of ^{182}Hf. Among hotspots, Hawaii, Iceland, Samoa, and Galápagos have the highest measured ^{3}He/^{4}He ratios (Kurz *et al.*, 1983, 2009; Hilton *et al.*, 1999; Jackson *et al.*, 2007) and the most solar-like Ne isotopes (Valbracht *et al.*, 1997; Trieloff *et al.*, 2000; Kurz *et al.*, 2009; Mukhopadhyay, 2012; Peto, Mukhopadhyay and Kelley, 2013; Jackson *et al.*, 2020; Péron *et al.*, 2021). Some of the strongest negative μ^{182}W anomalies occur in samples with high ^{3}He/^{4}He ratios from these same hotspots (Mundl *et al.*, 2017; Mundl-Petermeier *et al.*, 2020) (see Fig. 7).

The helium and neon isotopic signatures of the mega-ULVZ affiliated hotspots suggest a relatively undegassed source, which is commonly suggested to come from a deep mantle reservoir (Allègre *et al.*, 1983; Parai *et al.*, 2019), but has also been suggested to originate from the outer core (Bouhifd *et al.*, 2020). Xe isotopes measured in samples with high ^{3}He/^{4}He and solar-like Ne from Iceland and Samoa require that the reservoir that hosts this signature separated from the upper mantle within the first ~100 Myr of Earth history (Mukhopadhyay, 2012; Peto, Mukhopadhyay and Kelley, 2013). The anomalous tungsten isotope signature (negative μ^{182}W) suggests the involvement of a siderophile-enriched reservoir that likewise formed early in Earth's history. An obvious candidate for this reservoir is the core, and many potential processes to transfer material or isotopic signatures across the core-mantle boundary have been proposed (Buffett, Garnero and Jeanloz, 2000; Kanda and Stevenson, 2006; Hayden and Watson, 2007; Otsuka and Karato, 2012; Lesher *et al.*, 2020; Lim, Bonati and Hernlund, 2021). However, direct material transfer from the core would impart strongly fractionated noble gas elemental ratios to a plume, and these are not observed (Wang *et al.*, 2022). An alternative is an early-formed, iron-rich deep mantle reservoir. (Mundl-Petermeier *et al.*, 2020) suggests that to explain the full space of helium-tungsten isotope observations, two high ^{3}He/^{4}He components are needed: one with negative μ^{182}W and one with tungsten isotopes similar to the bulk silicate Earth. These distinct components could potentially reflect material entrainment from an LLVP and a ULVZ, with the ULVZ providing the negative tungsten isotope signature. Geodynamical modelling shows mantle plumes can sample LLVP material, and to a degree the much denser ULVZ material (Jones, Davies and Sossi, 2019). The correlation between these mega-ULVZs and the isotopic signatures is striking and should be tested in further localities.

4. Conclusions

We present seismic evidence of a mega-ULVZ on the core-mantle boundary to the west of the Galápagos in the form of postcursors to the Sdiff phase. Modeling the delay times and move-out of the postcursors allows us to constrain a simplified cylindrical shape with a width of ~600 km, a height of 20 km, a shear wave velocity reduction of 25%, and centered at 105º W and 2º N. This model also largely reproduces the observed incoming directionality of the postcursors. Similar mega-ULVZs have been mapped beneath or near the Hawaiian, Samoan and Icelandic

hotspots. Ocean island basalts in all four locations show anomalous signatures in He, Ne, and W, which could be clues to the mega-ULVZs representing a primordial reservoir or containing a component of outer core material.

Acknowledgements

The authors thank Curtis Williams, Helen Williams, and Vedran Lekic for discussion of this work. SC, CM, and ZL were funded by the European Research Council (ERC) under the European Union's Horizon 2020 research and innovation programme (grant agreement No. 804071 -ZoomDeep). RP was funded by National Science Foundation grant EAR 2145663. This work was performed using resources provided by the Cambridge Service for Data Driven Discovery (CSD3) operated by the University of Cambridge Research Computing Service (www.csd3.cam.ac.uk).

Data and code availability

The facilities of IRIS Data Services (www.iris.edu), and specifically the IRIS Data Management Center, were used for access to waveforms and related metadata. IRIS Data Services are funded through the Seismological Facilities for the Advancement of Geoscience (SAGE) Award of the National Science Foundation under Cooperative Support Agreement EAR-1851048. Data from the TA network were made freely available as part of the EarthScope USArray facility, operated by Incorporated Research Institutions for Seismology (IRIS) and supported by the National Science Foundation, under Cooperative Agreements EAR-1261681. Earthquake parameters were used from the Global CMT Project (www.globalcmt.org) and USGS National Earthquake Information Centre (earthquake.usgs.gov). Codes used will be made available by SC or CM upon request.

Competing interests

Authors declare that they have no competing interests.

References

Allègre, C. J. *et al.* (1983) 'Constraints on evolution of Earth's mantle from rare gas systematics', *Nature*. Nature Publishing Group, 303(5920), pp. 762–766. doi: 10.1038/303762a0.

Bouhifd, M. A. *et al.* (2020) 'Potential of earth's core as a reservoir for noble gases: Case for helium and neon', *Geochemical Perspectives Letters*, 15, pp. 15–18. doi: 10.7185/geochemlet.2028.

Buffett, B. A., Garnero, E. J. and Jeanloz, R. (2000) 'Sediments at the Top of Earth's Core', *Science*, 290(5495), pp. 1338–1342. doi: 10.1126/science.290.5495.1338.

Capdeville, Y. *et al.* (2002) 'A new coupled spectral element and modal solution method for global seismology: A first application to the scattering induced by a plume-like anomaly', *Geophysical Research Letters*, 29(9), pp. 32-1-32–4. doi: 10.1029/2001GL013747.

Capdeville, Y., To, A. and Romanowicz, B. (2003) 'Coupling spectral elements and modes in a

spherical Earth: an extension to the “sandwich” case’, *Geophysical Journal International*, 154(1), pp. 44–57. doi: 10.1046/j.1365-246X.2003.01959.x.

Cottaar, S. and Lekić, V. (2016) ‘Morphology of seismically slow lower-mantle structures’, *Geophys. J. Int.*, 207(2), pp. 1122–1136. doi: 10.1093/gji/ggw324.

Cottaar, S. and Romanowicz, B. (2012) ‘An unsually large ULVZ at the base of the mantle near Hawaii’, *Earth and Planetary Science Letters*, 355–356, pp. 213–222. doi: 10.1016/j.epsl.2012.09.005.

Dannberg, J. *et al.* (2021) ‘The morphology, evolution and seismic visibility of partial melt at the core-mantle boundary: Implications for ULVZs’, *Geophysical Journal International*, 227(2), pp. 1028–1059. doi: 10.1093/gji/ggab242.

Day, J. M. D., Jones, T. D. and Nicklas, R. W. (2022) ‘Mantle sources of ocean islands basalts revealed from noble gas isotope systematics’, *Chemical Geology*. Elsevier, 587, p. 120626. doi: 10.1016/j.chemgeo.2021.120626.

Dobrosavljevic, V. V., Sturhahn, W. and Jackson, J. M. (2019) ‘Evaluating the role of iron-rich (Mg,Fe)o in ultralow velocity zones’, *Minerals*. Multidisciplinary Digital Publishing Institute, 9(12), p. 762. doi: 10.3390/min9120762.

Domeier, M. *et al.* (2016) ‘Global correlation of lower mantle structure and past subduction’, *Geophysical Research Letters*. John Wiley & Sons, Ltd, 43(10), pp. 4945–4953. doi: 10.1002/2016GL068827.

Dziewonski, A. M. and Anderson, D. L. (1981) ‘Preliminary reference Earth model’, *Physics of the Earth and Planetary Interiors*, 25(4), pp. 297–356. doi: 10.1016/0031-9201(81)90046-7.

Ekström, G., Nettles, M. and Dziewoński, A. M. (2012) ‘The global CMT project 2004-2010: Centroid-moment tensors for 13,017 earthquakes’, *Physics of the Earth and Planetary Interiors*, 200–201, pp. 1–9. doi: 10.1016/j.pepi.2012.04.002.

French, S. W. and Romanowicz, B. (2015) ‘Broad plumes rooted at the base of the Earth’s mantle beneath major hotspots.’, *Nature*. Nature Publishing Group, a division of Macmillan Publishers Limited. All Rights Reserved., 525(7567), pp. 95–9. doi: 10.1038/nature14876.

French, S. W. and Romanowicz, B. A. (2014) ‘Whole-mantle radially anisotropic shear velocity structure from spectral-element waveform tomography’, *Geophysical Journal International*, 199(3), pp. 1303–1327. doi: 10.1093/gji/ggu334.

Garnero, E. J., McNamara, A. K. and Shim, S.-H. (2016) ‘Continent-sized anomalous zones with low seismic velocity at the base of Earth’s mantle’, *Nature Geosci.*, 9(7), pp. 481–489. doi: 10.1038/ngeo2733.

Geist, D. J., White, W. M. and McBirney, A. R. (1988) ‘Plume-asthenosphere mixing beneath the Galapagos archipelago’, *Nature*. Nature Publishing Group, 333(6174), pp. 657–660. doi: 10.1038/333657a0.

Gleeson, M. *et al.* (2021) ‘Geochemical Constraints on the Structure of the Earth’s Deep Mantle and the Origin of the LLSVPs’, *Geochemistry, Geophysics, Geosystems*. John Wiley & Sons, Ltd, 22(9). doi: 10.1029/2021GC009932.

Graham, D. W. *et al.* (1993) 'Mantle plume helium in submarine basalts from the Galápagos platform', *Science*. American Association for the Advancement of Science, 262(5142), pp. 2023–2026. doi: 10.1126/science.262.5142.2023.

Harper, C. L. and Jacobsen, S. B. (1996) 'Noble gases and earth's accretion', *Science*. American Association for the Advancement of Science, 273(5283), pp. 1814–1818. doi: 10.1126/science.273.5283.1814.

Harpp, K. S. and Weis, D. (2020) 'Insights Into the Origins and Compositions of Mantle Plumes: A Comparison of Galápagos and Hawai'i', *Geochemistry, Geophysics, Geosystems*. John Wiley & Sons, Ltd, 21(9). doi: 10.1029/2019GC008887.

Harpp, K. S. and White, W. M. (2001) 'Tracing a mantle plume: Isotopic and trace element variations of Galápagos seamounts', *Geochemistry, Geophysics, Geosystems*. John Wiley & Sons, Ltd, 2(6). doi: 10.1029/2000gc000137.

Hauser, J., Sambridge, M. and Rawlinson, N. (2008) 'Multiarrival wavefront tracking and its applications', *Geochemistry, Geophysics, Geosystems*. John Wiley & Sons, Ltd, 9(11). doi: 10.1029/2008GC002069.

Hayden, L. A. and Watson, E. B. (2007) 'A diffusion mechanism for core–mantle interaction', *Nature*. Nature Publishing Group, 450(7170), pp. 709–711. doi: 10.1038/nature06380.

Hernlund, J. W. and Jellinek, A. M. (2010) 'Dynamics and structure of a stirred partially molten ultralow-velocity zone', *Earth and Planetary Science Letters*, 296(1–2), pp. 1–8. doi: 10.1016/j.epsl.2010.04.027.

Van der Hilst, R. D., Widiyantoro, S. and Engdahl, E. R. (1997) 'Evidence for deep mantle circulation from global tomography', *Nature*. Nature Publishing Group, 386(6625), pp. 578–584. doi: 10.1038/386578a0.

Hilton, D. R. *et al.* (1999) 'Extreme 3He/4He ratios in northwest Iceland: Constraining the common component in mantle plumes', *Earth and Planetary Science Letters*. Elsevier, 173(1–2), pp. 53–60. doi: 10.1016/S0012-821X(99)00215-0.

Hosseini, K. *et al.* (2020) 'Global mantle structure from multifrequency tomography using P, PP and P-diffracted waves', *Geophysical Journal International*. Oxford Academic, 220(1), pp. 96–141. doi: 10.1093/gji/ggz394.

Jackson, M. G. *et al.* (2007) 'New Samoan lavas from Ofu Island reveal a hemispherically heterogeneous high 3He/4He mantle', *Earth and Planetary Science Letters*. Elsevier, 264(3–4), pp. 360–374. doi: 10.1016/j.epsl.2007.09.023.

Jackson, M. G. *et al.* (2020) 'Ancient helium and tungsten isotopic signatures preserved in mantle domains least modified by crustal recycling', *Proceedings of the National Academy of Sciences of the United States of America*, 117(49), pp. 30993–31001. doi: 10.1073/pnas.2009663117.

Jackson, M. G., Konter, J. G. and Becker, T. W. (2017) 'Primordial helium entrained by the hottest mantle plumes', *Nature*, 542(7641), pp. 340–343. doi: 10.1038/nature21023.

Jellinek, A. M. and Manga, M. (2004) 'Links between long-lived hot spots, mantle plumes, D'' , and plate tectonics', *Reviews of Geophysics*, 42(3), p. RG3002. doi: 10.1029/2003RG000144.

Jenkins, J. *et al.* (2021) 'A high-resolution map of Hawaiian ULVZ morphology from ScS phases', *Earth and Planetary Science Letters*, 563, p. 116885. doi: 10.1016/j.epsl.2021.116885.

Jones, T. D., Davies, D. R. and Sossi, P. A. (2019) 'Tungsten isotopes in mantle plumes: Heads it's positive, tails it's negative', *Earth and Planetary Science Letters*. Elsevier, 506, pp. 255–267. doi: 10.1016/J.EPSL.2018.11.008.

Kanda, R. V. S. and Stevenson, D. J. (2006) 'Suction mechanism for iron entrainment into the lower mantle', *Geophys. Res. Lett.*, 33(2), p. L02310. doi: 10.1029/2005GL025009.

Kim, D. *et al.* (2020) 'Sequencing seismograms: A panoptic view of scattering in the core-mantle boundary region', *Science*, 368(6496), pp. 1223–1228. doi: 10.1126/science.aba8972.

Kleine, T. *et al.* (2002) 'Rapid accretion and early core formation on asteroids and the terrestrial planets from Hf-W chronometry', *Nature*. Nature Publishing Group, 418(6901), pp. 952–955. doi: 10.1038/nature00982.

Kurz, M. D. *et al.* (1983) 'Helium isotopic variations in volcanic rocks from Loihi Seamount and the Island of Hawaii', *Earth and Planetary Science Letters*. Elsevier, 66(C), pp. 388–406. doi: 10.1016/0012-821X(83)90154-1.

Kurz, M. D. *et al.* (2009) 'Primitive neon from the center of the Galápagos hotspot', *Earth and Planetary Science Letters*. Elsevier, 286(1–2), pp. 23–34. doi: 10.1016/j.epsl.2009.06.008.

Kurz, M. D. and Geist, D. (1999) 'Dynamics of the Galapagos hotspot from helium isotope geochemistry', *Geochimica et Cosmochimica Acta*. Pergamon, 63(23–24), pp. 4139–4156. doi: 10.1016/s0016-7037(99)00314-2.

Labrosse, S., Hernlund, J. W. and Coltice, N. (2007) 'A crystallizing dense magma ocean at the base of the Earth's mantle.', *Nature*, 450(7171), pp. 866–9. doi: 10.1038/nature06355.

Lai, V. H. *et al.* (2022) 'Strong ULVZ and Slab Interaction at the Northeastern Edge of the Pacific LLSVP Favors Plume Generation', *Geochemistry, Geophysics, Geosystems*, 23(2). doi: 10.1029/2021gc010020.

Lei, W. *et al.* (2020) 'Global adjoint tomography - Model GLAD-M25', *Geophysical Journal International*. Oxford Academic, 223(1), pp. 1–21. doi: 10.1093/gji/ggaa253.

Lesher, C. E. *et al.* (2020) 'Iron isotope fractionation at the core–mantle boundary by thermodiffusion', *Nature Geoscience*. Nature Publishing Group, 13(5), pp. 382–386. doi: 10.1038/s41561-020-0560-y.

Li, J., Sun, D. and Bower, D. J. (2022) 'Slab control on the mega-sized North Pacific ultra-low velocity zone', *Nature Communications*, 13(1), p. 1042. doi: 10.1038/s41467-022-28708-8.

Li, M. *et al.* (2017) 'Compositionally-distinct ultra-low velocity zones on Earth's core-mantle boundary.', *Nature comm.*, 8(1), p. 177. doi: 10.1038/s41467-017-00219-x.

Li, M. and Zhong, S. (2017) 'The source location of mantle plumes from 3D spherical models of mantle convection', *Earth and Planetary Science Letters*. Elsevier, 478, pp. 47–57. doi: 10.1016/J.EPSL.2017.08.033.

Li, Z. *et al.* (2022) 'Kilometer-scale structure on the core–mantle boundary near Hawaii', *Nature Communications*, 13(1), p. 2787. doi: 10.1038/s41467-022-30502-5.

Lim, K. W., Bonati, I. and Hernlund, J. W. (2021) 'A Hybrid Mechanism for Enhanced Core-Mantle Boundary Chemical Interaction', *Geophysical Research Letters*. John Wiley & Sons, Ltd, 48(23). doi: 10.1029/2021GL094456.

Ma, X., Sun, X. and Thomas, C. (2019) 'Localized ultra-low velocity zones at the eastern boundary of Pacific LLSVP', *Earth and Planetary Science Letters*. Elsevier, 507, pp. 40–49. doi: 10.1016/J.EPSL.2018.11.037.

Mukhopadhyay, S. (2012) 'Early differentiation and volatile accretion recorded in deep-mantle neon and xenon', *Nature*. Nature Publishing Group, 486(7401), pp. 101–104. doi: 10.1038/nature11141.

Mukhopadhyay, S. and Parai, R. (2019) 'Noble gases: A record of earth's evolution and mantle dynamics', *Annual Review of Earth and Planetary Sciences*. Annual Reviews, pp. 389–419. doi: 10.1146/annurev-earth-053018-060238.

Mundl-Petermeier, A. *et al.* (2020) 'Anomalous 182W in high 3He/4He ocean island basalts: Fingerprints of Earth's core?', *Geochimica et Cosmochimica Acta*, 271, pp. 194–211. doi: 10.1016/j.gca.2019.12.020.

Mundl, A. *et al.* (2017) 'Tungsten-182 heterogeneity in modern ocean island basalts.', *Science*, 356(6333), pp. 66–69. doi: 10.1126/science.aal4179.

Nolet, G. *et al.* (2019) 'Imaging the Galápagos mantle plume with an unconventional application of floating seismometers', *Scientific Reports*. Nature Publishing Group, 9(1), p. 1326. doi: 10.1038/s41598-018-36835-w.

Otsuka, K. and Karato, S. I. (2012) 'Deep penetration of molten iron into the mantle caused by a morphological instability', *Nature*. Nature Publishing Group, 492(7428), pp. 243–246. doi: 10.1038/nature11663.

Parai, R. *et al.* (2019) 'The emerging portrait of an ancient, heterogeneous and continuously evolving mantle plume source', *Lithos*. Elsevier, p. 105153. doi: 10.1016/j.lithos.2019.105153.

Péron, S. *et al.* (2021) 'Deep-mantle krypton reveals Earth's early accretion of carbonaceous matter', *Nature*. Nature Publishing Group, 600(7889), pp. 462–467. doi: 10.1038/s41586-021-04092-z.

Peters, B. J. *et al.* (2021) 'Combined Lithophile-Siderophile Isotopic Constraints on Hadean Processes Preserved in Ocean Island Basalt Sources', *Geochemistry, Geophysics, Geosystems*. John Wiley & Sons, Ltd, 22(3). doi: 10.1029/2020GC009479.

Peto, M. K., Mukhopadhyay, S. and Kelley, K. A. (2013) 'Heterogeneities from the first 100 million years recorded in deep mantle noble gases from the Northern Lau Back-arc Basin', *Earth and Planetary Science Letters*. Elsevier, 369–370, pp. 13–23. doi: 10.1016/j.epsl.2013.02.012.

Rizo, H. *et al.* (2019) '182W evidence for core-mantle interaction in the source of mantle plumes', *Geochemical Perspectives Letters*, 11, pp. 6–11. doi: 10.7185/geochemlet.1917.

Rost, S. and Thomas, C. (2002) 'Array seismology: Methods and applications', *Reviews of Geophysics*, 40(3), p. 1008. doi: 10.1029/2000RG000100.

Schimmel, M. and Paulssen, H. (1997) 'Noise reduction and detection of weak, coherent signals

through phase-weighted stacks', *Geophysical Journal International*. Oxford Academic, 130(2), pp. 497–505. doi: 10.1111/j.1365-246X.1997.tb05664.x.

Steinberger, B. and Torsvik, T. H. (2012) 'A geodynamic model of plumes from the margins of Large Low Shear Velocity Provinces', *Geochemistry, Geophysics, Geosystems*, 13(1), p. n/a-n/a. doi: 10.1029/2011GC003808.

Thorne, M. S. *et al.* (2013) 'Mega ultra low velocity zone and mantle flow', *Earth and Planetary Science Letters*, 364, pp. 59–67. doi: 10.1016/j.epsl.2012.12.034.

Trieloff, M. *et al.* (2000) 'The nature of pristine noble gases in mantle plumes', *Science*. American Association for the Advancement of Science, 288(5468), pp. 1036–1038. doi: 10.1126/science.288.5468.1036.

Valbracht, P. J. *et al.* (1997) 'Noble gas systematics of deep rift zone glasses from Loihi Seamount, Hawaii', *Earth and Planetary Science Letters*. Elsevier, 150(3–4), pp. 399–411. doi: 10.1016/s0012-821x(97)00094-0.

Wang, K. *et al.* (2022) 'Partitioning of noble gases (He, Ne, Ar, Kr, Xe) during Earth's core segregation: A possible core reservoir for primordial noble gases', *Geochimica et Cosmochimica Acta*. Pergamon, 321, pp. 329–342. doi: 10.1016/j.gca.2022.01.009.

White, W. M., McBirney, A. R. and Duncan, R. A. (1993) 'Petrology and geochemistry of the Galapagos Islands: portrait of a pathological mantle plume', *Journal of Geophysical Research*. John Wiley & Sons, Ltd, 98(B11), pp. 19533–19563. doi: 10.1029/93jb02018.

Wicks, J. K. *et al.* (2017) 'Sound velocity and density of magnesiowüstites: Implications for ultralow-velocity zone topography', *Geophysical Research Letters*. John Wiley & Sons, Ltd, 44(5), pp. 2148–2158. doi: 10.1002/2016GL071225.

Williams, C. D. *et al.* (2019) 'Primitive Helium Is Sourced From Seismically Slow Regions in the Lowermost Mantle', *Geochemistry, Geophysics, Geosystems*. John Wiley & Sons, Ltd, 20(8), pp. 4130–4145. doi: 10.1029/2019GC008437.

Yin, Q. *et al.* (2002) 'A short timescale for terrestrial planet formation from Hf-W chronometry of meteorites', *Nature*. Nature Publishing Group, 418(6901), pp. 949–952. doi: 10.1038/nature00995.

Yu, S. and Garnero, E. J. (2018) 'Ultralow Velocity Zone Locations: A Global Assessment', *Geochemistry, Geophysics, Geosystems*. John Wiley & Sons, Ltd, 19(2), pp. 396–414. doi: 10.1002/2017GC007281.

Yuan, K. and Romanowicz, B. (2017) 'Seismic evidence for partial melting at the root of major hot spot plumes.', *Science (New York, N.Y.)*. American Association for the Advancement of Science, 357(6349), pp. 393–397. doi: 10.1126/science.aan0760.

The root to the Galápagos mantle plume on the core-mantle boundary - supplementary materials

Sanne Cottaar[1]*, Carl Martin[1], Zhi Li[1], Rita Parai[2]

1. Department of Earth Sciences, University of Cambridge, Cambridge, UK
2. Department of Earth and Planetary Sciences, Washington University in St Louis, St Louis, MO, USA

* corresponding author: sc845@cam.ac.uk

This PDF file includes:

Additional text

Figs. S1 to S14

Table S1

Other Supplementary Materials for this manuscript include the following:

Movies S1 to S4 – available at https://doi.org/10.5281/zenodo.6783206

1. Sdiff postcursor data set

Several further examples of events with postcursors are presented here. Fig. S1 shows the waveforms for an earthquake along the Chilean subduction zone on 2020/11/03. The event geometry is comparable to events A and B, and like with these events, postcursors are present presenting a moveout in time towards larger azimuths. The data for this event are very noisy, and the event is therefore excluded from further modelling. Additionally, the 1D synthetics show that the waveforms predicted are not a great fit, and the earthquake depth or the relative amplitudes between the direct and depth phases would have to be adjusted.

Postcursors caused by the Galápagos ULVZ are also seen after ScS phases. Fig. S2 shows an example of S/ScS waveforms in the 85-95° distance range from an earthquake at Easter Island recorded at stations in the United States and Canada. Postcursors in this distance range require further exploration and modelling beyond the scope of this study.

In Figs. S3 and S4, the geometry and waveforms are shown for three events in Alaska recorded across southern South America, which is a geometry largely opposite to events A and B. Waveform quality is generally poor and station coverage is sparser than in the opposite direction. Synthetic waveforms for the preferred ULVZ model are shown to suggest were postcursors might be present, and hints of these can be observed. Particularly the data for event T suggests a

postcursor that appears further delayed in time than is observed in the synthetic data. This could be evidence that the ULVZ needs to be more asymmetric than the simplified cylindrical model presented here.

2. Trade-offs in forward modelling

In the main paper we present our preferred cylindrical ULVZ model. Here we illustrate the sensitivity of the data to location, size, velocity reduction, and height of the model. Unlike several studies using diffracted data (Yuan and Romanowicz, 2017; Li, Sun and Bower, 2022), we have not been able to devise a quantitative measure to compare different models for several reasons. For event A, this is likely due to the overall poor waveform fit between the data and synthetic, which is controlled by the depth and source time function of the earthquake source and has not been optimized for this subset of data. For event B, the postcursor is weak and does not dominate any waveform misfit. For event C, we do not fit the amplitude of the postcursor well but fit the overall character. This could be due to our simplified model choices, or due to the assumed earthquake source. For event D, the data coverage is too poor to track and fit particular postcursors.

Forward modelling – location

The preferred cylindrical ULVZ model is centered at 105º W and 2º N, to the west of the Galápagos. Its location is constrained by having crossing ray paths from the different events. We illustrate this by presenting synthetics for shifted ULVZ models (Fig. S5) for event A (Fig. S6) and event C (Fig. S7). Event A samples the ULVZ from the southeast to the northwest, and synthetic models are presented shifted in these directions (labelled as SE and NW). In Fig. S6, we observe that the synthetic waveforms for these models remain comparable when shifted in these directions. Waveforms for synthetic models shifted in the orthogonal direction (labelled as SW and NE) show stronger variations in both postcursor moveout and amplitude.

For event C, the direction of propagation aligns the models SW and NW, and the models SE and NE. We observe little difference in the waveforms between SW and NW, or between SE and NE, but the move-out and amplitudes are very different between them. Postcursors for models to the west are offset towards smaller azimuth and for models to the east to larger azimuths than observed in the data. The combination of the two events thus constrains the best location within uncertainty of about 2º.

Forward modelling – size and velocity reduction

Size and velocity reduction are the least well constrained. Based purely on travel-times we expect strong trade-offs: a smaller and more reduced ULVZ predicts nearly the same postcursor travel time delays as a larger and less reduced ULVZ. When modelling we can observe more subtle waveform variations for differently sized ULVZs. Figs. S8 and S9 show comparisons for different velocity reductions and ULVZ widths for events A and B. We compare modified models to the preferred model with a velocity reduction of 25% and a width of 600 km. In both cases, we observe that models with a weaker velocity reduction and a smaller width show a less strong move-out in the postcursors, while the move-out is too strong when the velocity reduction or width are increased. For event B, we also observe a strong variation in amplitude, with the postcursor almost disappearing for the weaker or smaller models.

More comparable waveforms can be obtained when both velocity reduction and width are varied inversely at the same time. Therefore, the uncertainties are the velocity reduction are at least 5% and the width is at least 100 km.

Forward modelling – height

To evaluate the height, we assess the data at longer periods between 30 to 50s. At these periods, the amplitudes and travel-time delays of the observed postcursors are reduced. Event A (Fig. S10) still shows significant postcursors, but postcursors are barely visible for Events B and C (Figs. S11 and S12). This comparison is reproduced by synthetics with a ULVZ height of 20 km. For larger ULVZs, postcursor amplitudes increase significantly. There will be some trade-off with the overall size and velocity reduction of the ULVZ, and we expect equally fitting models can be found with 15 or 25 km thick ULVZs.

3. Beamforming results

For event A, we found 15 high quality stack windows for which the results are shown in Fig. 6, where they are compared to the results from the same stacking procedure on the synthetic data for our preferred ULVZ model. An example of a high-quality stack for event A is shown in Fig. S13. Event C has 13 high quality stacks for which 6 have a postcursor. Results for event C are shown in Fig. S14, comparing the results of observed stacks to those for the synthetic data of the preferred ULVZ model. In both cases, a bimodal distribution of peaks with time and backazimuth is observed. The synthetics for our preferred model slightly overpredict the difference in backazimuth between the main phases and the postcursors.

Event B has very little significant energy in the postcursor, as is also clear from the waveforms, and is therefore not further considered. Event D does not have sufficient coverage for stations with potential postcursors to consider stacking.

References

Dziewonski, A. M. and Anderson, D. L. (1981) 'Preliminary reference Earth model', *Physics of the Earth and Planetary Interiors*, 25(4), pp. 297–356. doi: 10.1016/0031-9201(81)90046-7.

Ekström, G., Nettles, M. and Dziewoński, A. M. (2012) 'The global CMT project 2004-2010: Centroid-moment tensors for 13,017 earthquakes', *Physics of the Earth and Planetary Interiors*, 200–201, pp. 1–9. doi: 10.1016/j.pepi.2012.04.002.

French, S. W. and Romanowicz, B. A. (2014) 'Whole-mantle radially anisotropic shear velocity structure from spectral-element waveform tomography', *Geophysical Journal International*, 199(3), pp. 1303–1327. doi: 10.1093/gji/ggu334.

Hauser, J., Sambridge, M. and Rawlinson, N. (2008) 'Multiarrival wavefront tracking and its applications', *Geochemistry, Geophysics, Geosystems*. John Wiley & Sons, Ltd, 9(11). doi: 10.1029/2008GC002069.

Li, J., Sun, D. and Bower, D. J. (2022) 'Slab control on the mega-sized North Pacific ultra-low velocity zone', *Nature Communications*, 13(1), p. 1042. doi: 10.1038/s41467-022-28708-8.

Yuan, K. and Romanowicz, B. (2017) 'Seismic evidence for partial melting at the root of major hot spot plumes.', *Science (New York, N.Y.)*. American Association for the Advancement of Science, 357(6349), pp. 393–397. doi: 10.1126/science.aan0760.

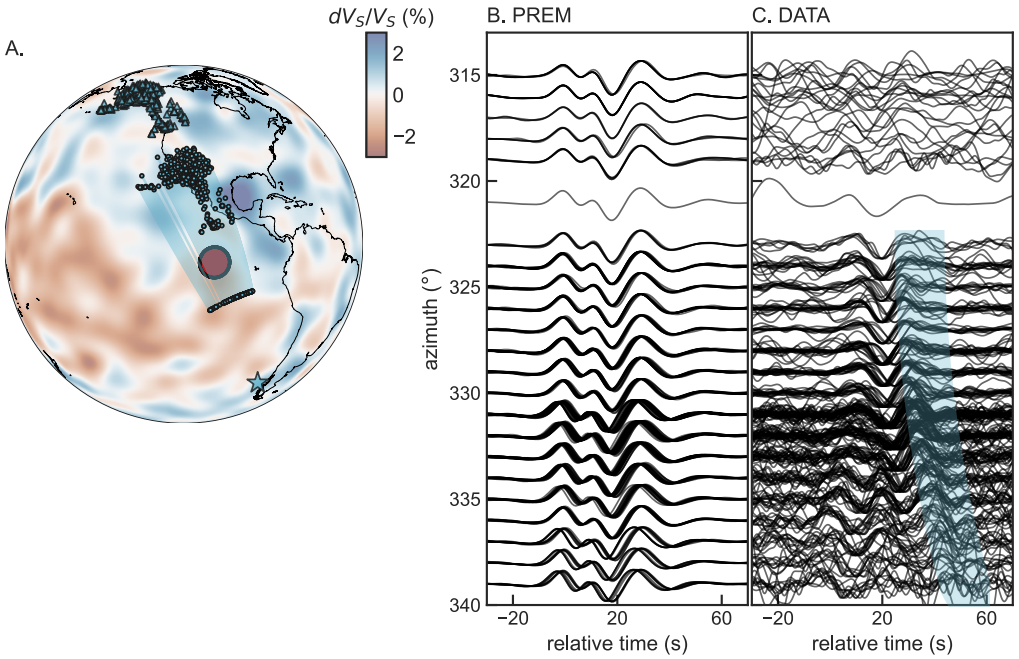

Fig. S1. Geometry and data for event on 2020/11/03.
(A) Map showing earthquake location (star), Sdiff paths in the lowermost mantle (shaded region) and stations (triangles). Preferred ULVZ shown in red. Background shows the shear wave velocity deviations at 2800 km depth from the tomographic SEMUCB-WM1 (French and Romanowicz, 2014). **(B)** Synthetic waveform predictions for PREM (Dziewonski and Anderson, 1981). **(C)** Observed waveforms. All waveforms are filtered between periods of 12 and 30 s. The geometry of this event is similar to event A and B in the main paper, but observations are noisier and the predicted waveforms are a poor fit.

825

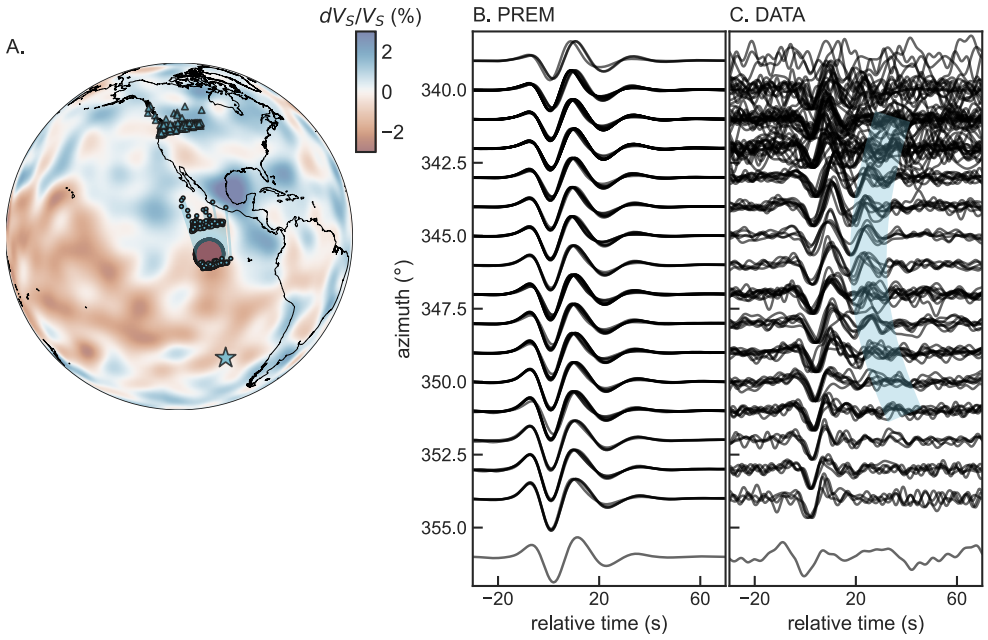

Fig. S2. Geometry and data for event on 2008/11/22.
(A) Map showing earthquake location (star), Sdiff paths in the lowermost mantle (shaded region) and stations (triangles). Preferred ULVZ shown in red. Background shows the shear wave
830 velocity deviations at 2800 km depth from the tomographic SEMUCB-WM1 (French and Romanowicz, 2014). **(B)** Synthetic waveform predictions for PREM (Dziewonski and Anderson, 1981). **(C)** Observed waveforms. All data are filtered between 10 and 30s. Data for this event are in the 85-95° distance range and postcursors are present to the S/ScS phases. Presence of postcursors at these shorter distances requires further investigation.

835

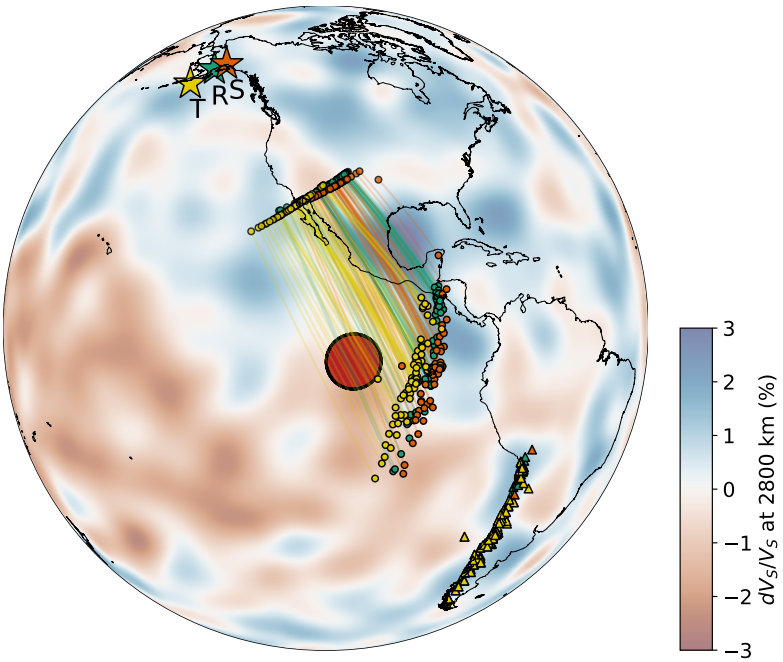

Fig. S3. Map of geometries for Alaska Events recorded in southern South America. Data geometries are shown by earthquake location (star), station locations (triangles), and ray path sensitivity to the core-mantle boundary (shaded regions between piercing points at 2800 km depth). Earthquake locations, ray paths and stations are coloured per event: R- cyan, S-orange, and T-yellow. The location of the Galápagos ULVZ, as constrained in this study, is shown as the red-filled circle. Background model shows the shear wave velocity deviations at 2800 km depth from the tomographic SEMUCB-WM1 (French and Romanowicz, 2014).

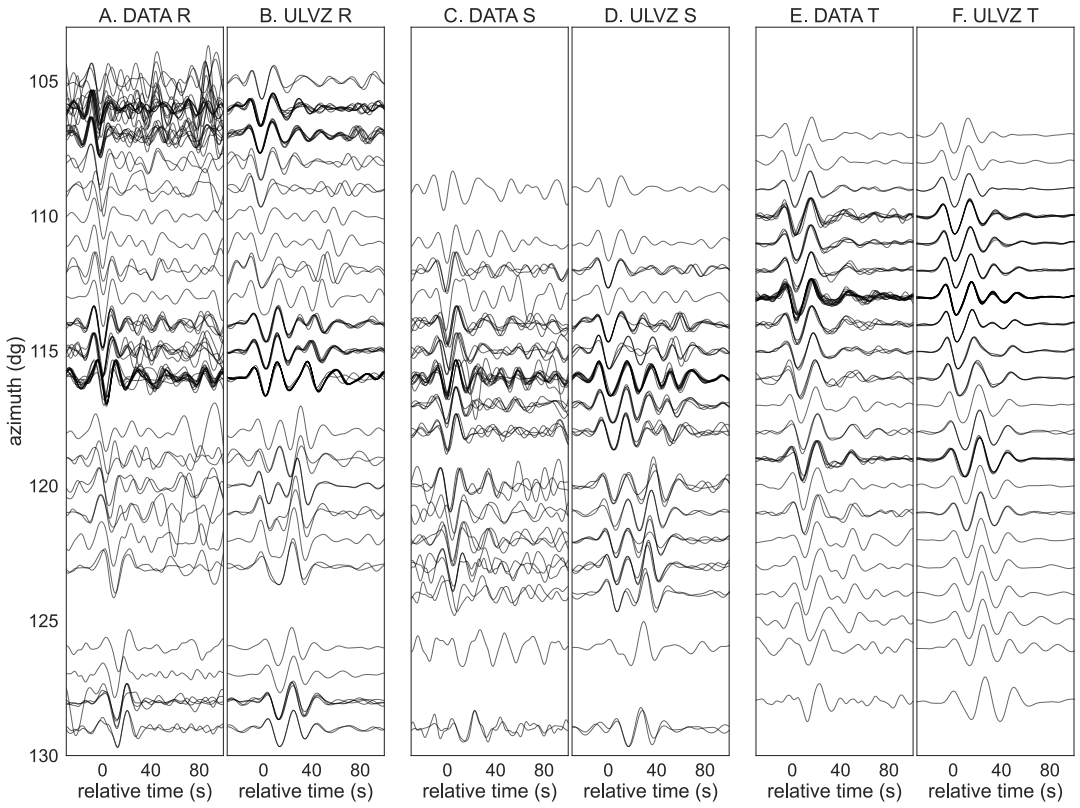

Fig. S4. Waveform data and synthetics for Alaska Events recorded in southern South America.
(A) Data for event R (2016/01/24) centered on the sSdiff phase, which is stronger than the main Sdiff phase for this event **(B)** corresponding synthetics for the preferred Galápagos ULVZ model. **(C.)** Data for event S (2018/11/30) centered on the sSdiff phase, which is stronger than the main Sdiff phase for this event **(D)** corresponding synthetics for the preferred ULVZ model. **(E)** Data for event R (2021/08/14) centered on the Sdiff phase, **(F)** corresponding synthetics for the preferred ULVZ model. All waveforms are filtered between 12.5 and 30 s. Data are relatively noisy, but hints of postcursors exist. Event T suggests the postcursor is further delayed than predicted by our preferred model.

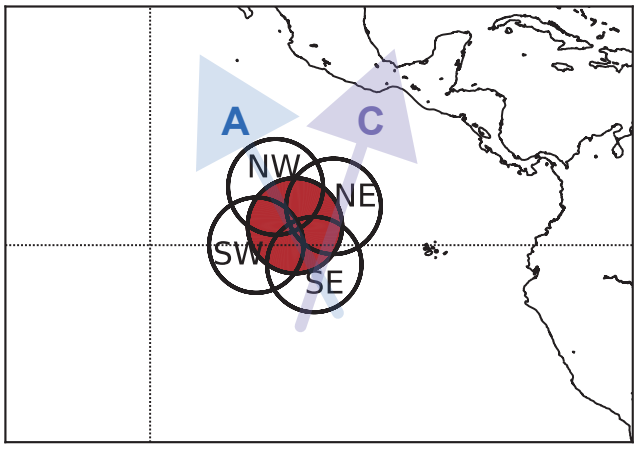

Fig. S5 Location shifts for the Galápagos ULVZ.
Reference preferred model is in red, centered at 105º W and 2º N. Shifted models are denoted as NW, NE, SE, and SW, indicating their shift directions. Arrows show the rough propagation direction for data for Event A (blue) and C (purple). ULVZ width of 600 km, height of 20 km, and shear wave velocity reduction of 25% are kept constant.

870

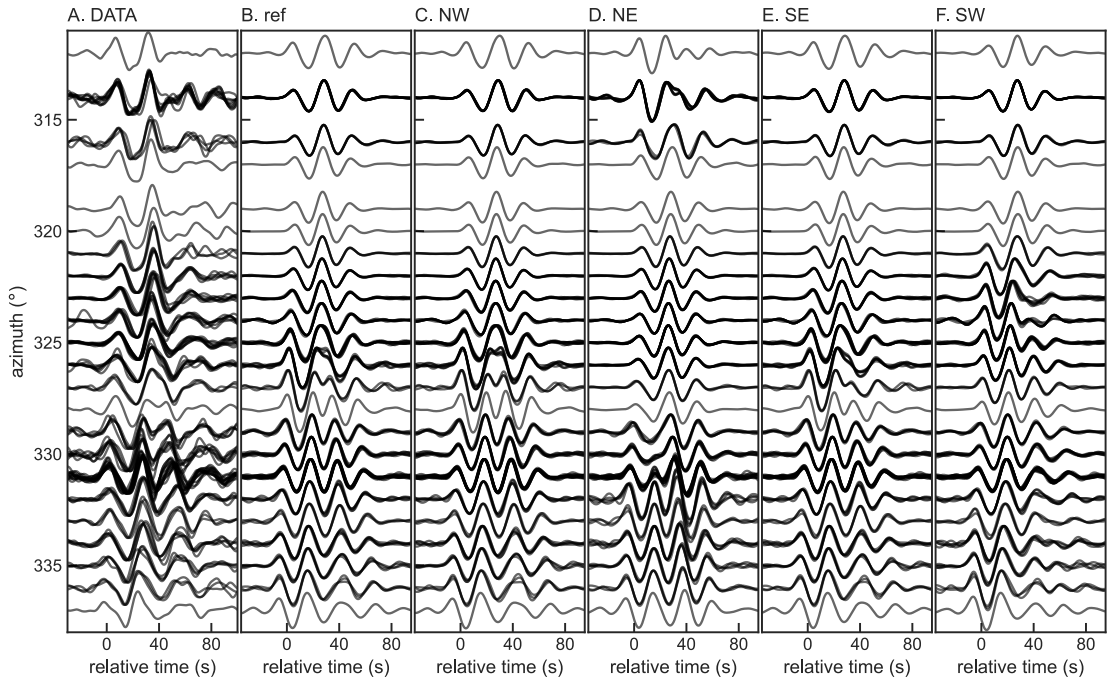

Fig. S6 Waveforms with location of the ULVZ for event A.
(A) Observed data for event A. **(B)** Synthetics for the preferred Galápagos ULVZ model. **(C)**
875 Synthetics for preferred model shifted to the NW. **(D)** Synthetics for preferred model shifted to the NE. **(E)** Synthetics for preferred model shifted to the SE. **(F)** Synthetics for preferred model shifted to the SW. See locations in Figure S5. All waveforms are filtered between periods of 10 and 30 s.

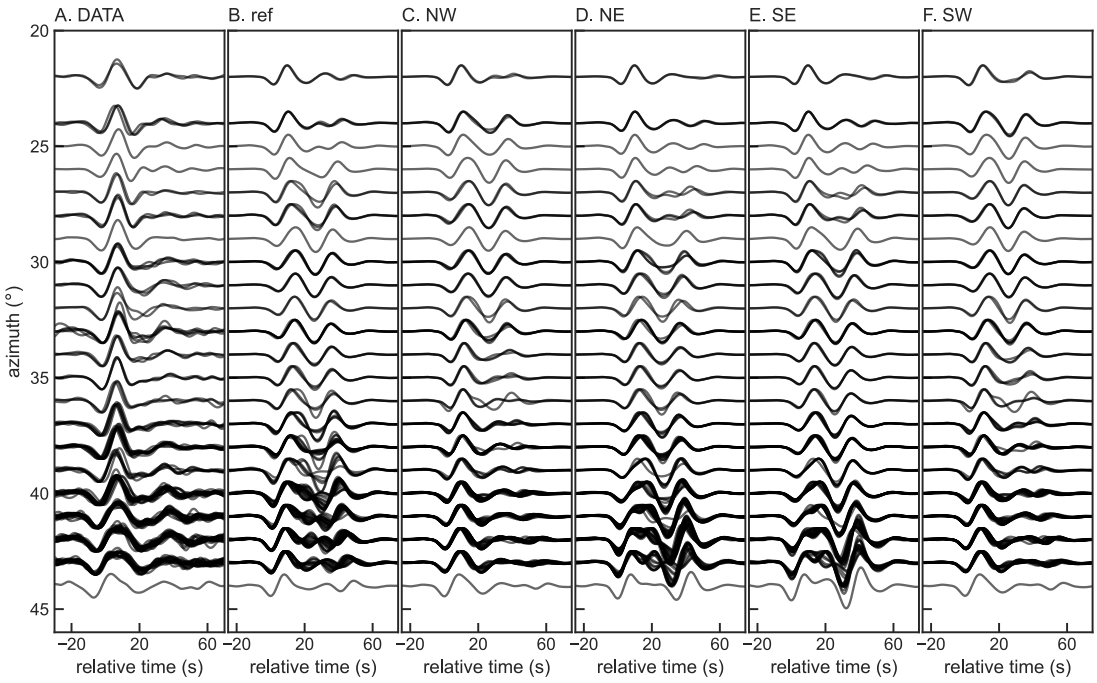

Fig. S7 Waveforms with location of the ULVZ for event C.
(A) Observed data for event C. **(B)** Synthetics for the preferred Galápagos ULVZ model. **(C)** Synthetics for preferred model shifted to the NW. **(D)** Synthetics for preferred model shifted to the NE. **(E)** Synthetics for preferred model shifted to the SE. **(F)** Synthetics for preferred model shifted to the SW. See locations in Figure S5. All waveforms are filtered between periods of 10 and 30 s.

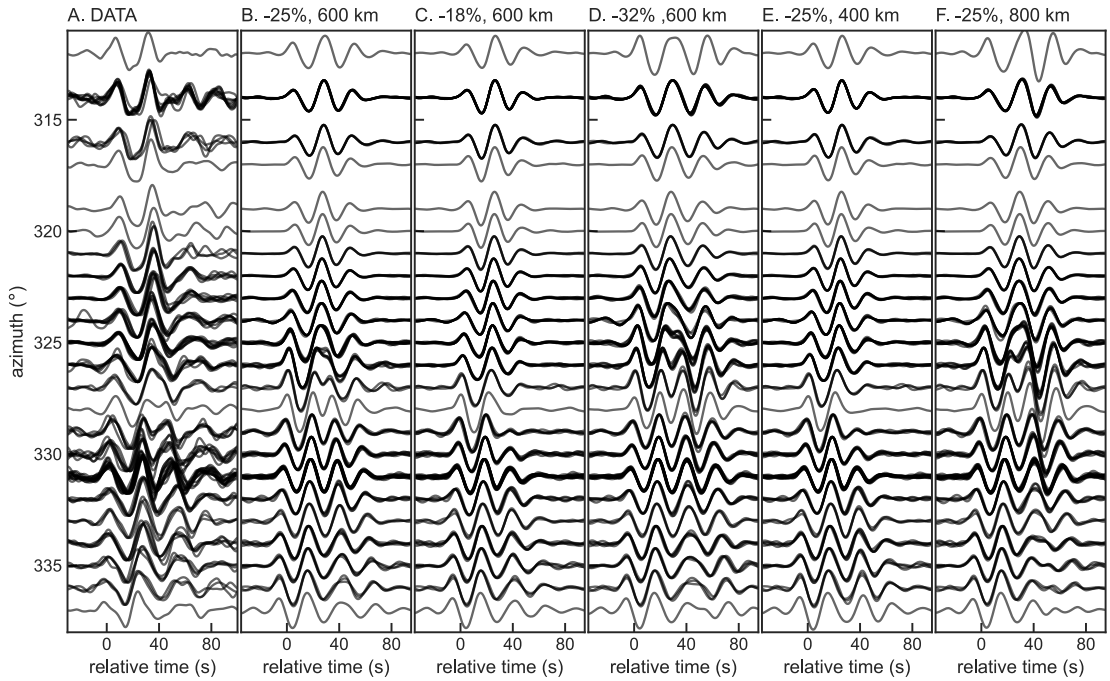

Fig. S8 Waveforms with varying velocity reduction and size of the ULVZ for event A.
(A) Observed data for event A. **(B)** Synthetics for the preferred Galápagos ULVZ model with a shear velocity reduction of 25% and a width of 600 km. **(C)** Synthetics for model with a smaller velocity reduction of 18%. **(D)** Synthetics for model with a larger velocity reduction of 32%. **(E)** Synthetics for a model with a width of 400 km. **(F)** Synthetics for a model with a width of 800 km. All waveforms are filtered between periods of 10 and 30 s.

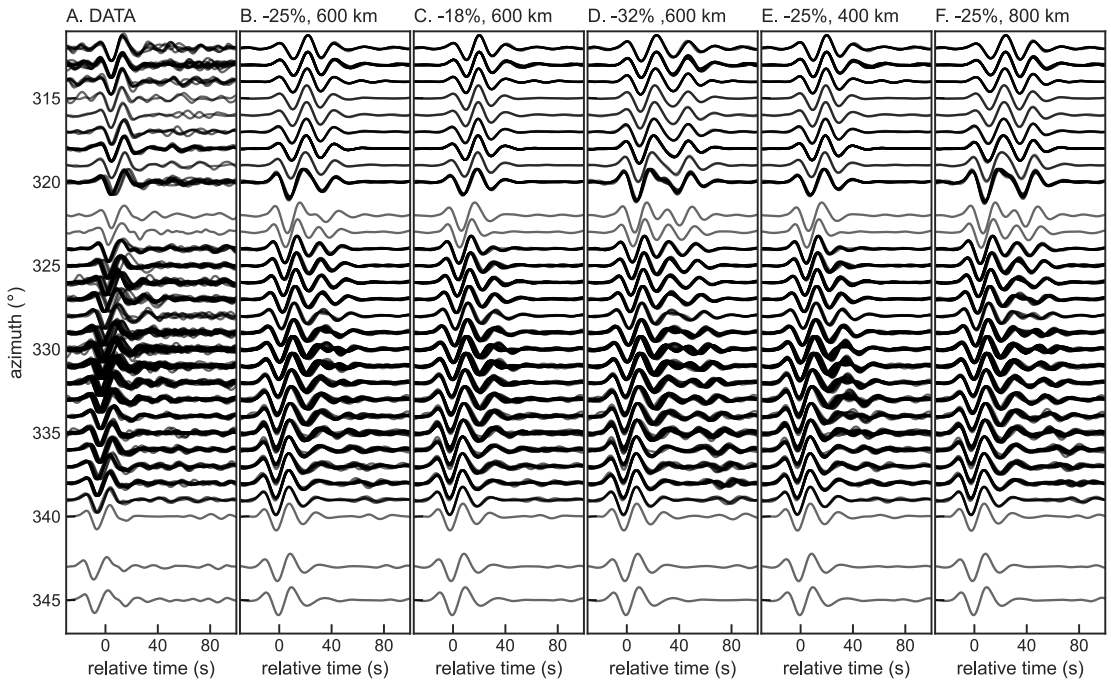

Fig. S9 Waveforms with varying velocity reduction and size of the ULVZ for event B. **(A)** Observed data for event B. **(B)** Synthetics for the preferred Galápagos ULVZ model with a shear velocity reduction of 25% and a width of 600 km. **(C)** Synthetics for model with a smaller velocity reduction of 18%. **(D)** Synthetics for model with a larger velocity reduction of 32%. **(E)** Synthetics for a model with a width of 400 km. **(F)** Synthetics for a model with a width of 800 km. All waveforms are filtered between periods of 10 and 30 s.

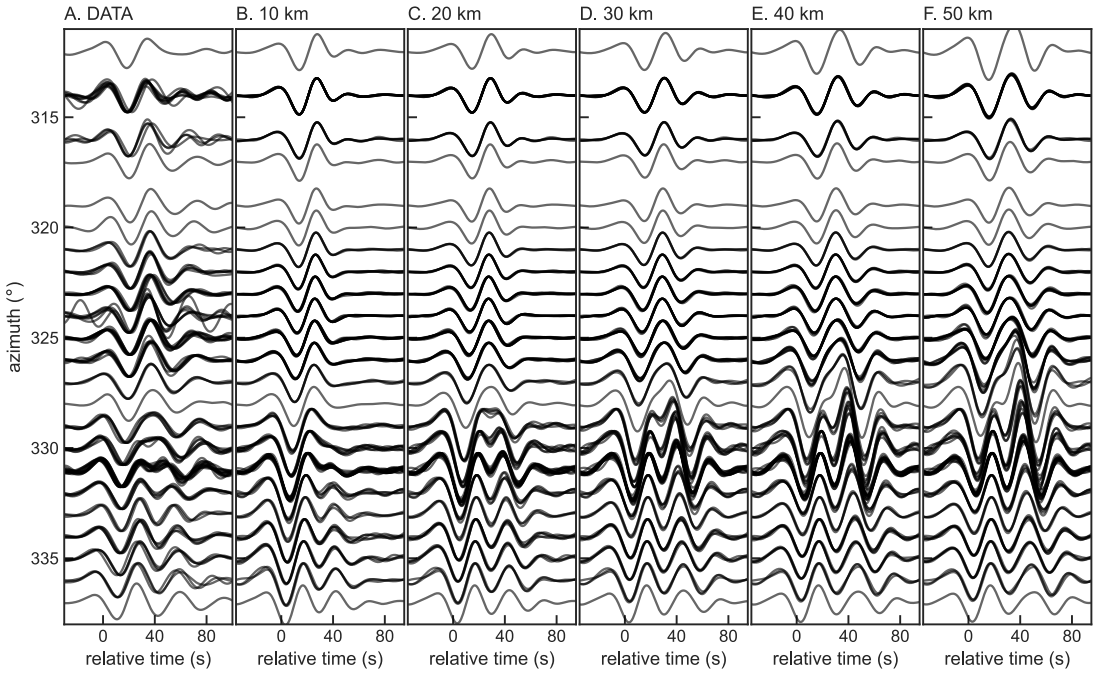

Fig. S10 Waveform predictions with height of the ULVZ for event A.
(A) Observed Sdiff waveforms. **(B-F)** Synthetic waveforms for ULVZs with a height of 10, 20, 30, 40, and 50 km. All waveforms filtered between periods of 30 and 50 s. The preferred model is 20 km in height.

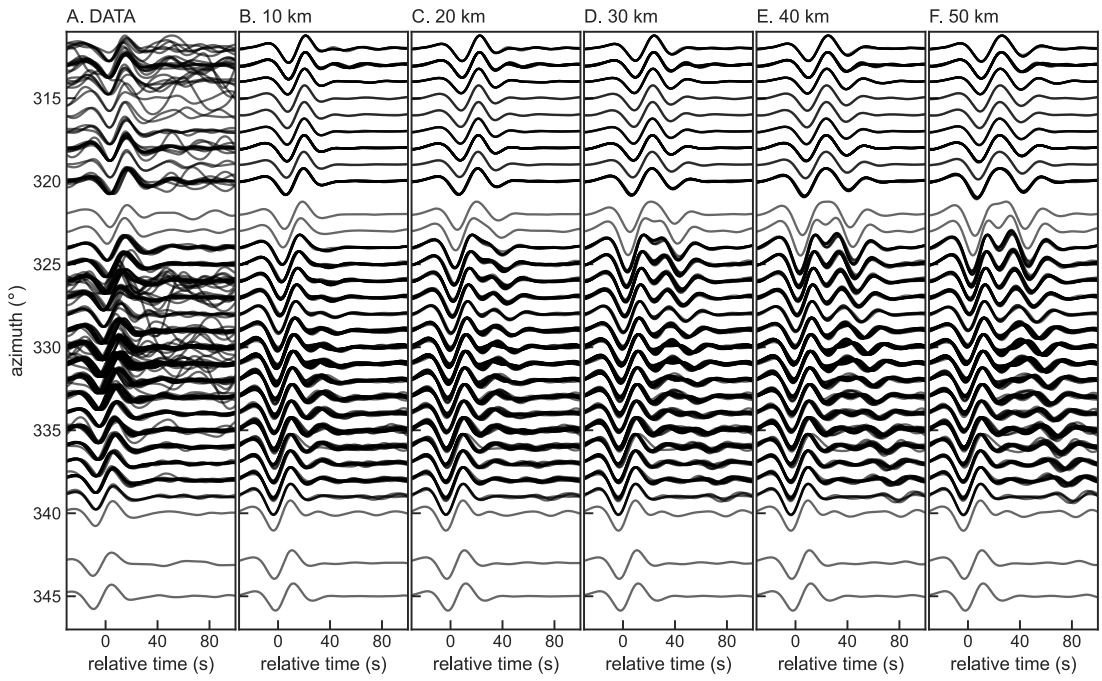

Fig. S11 Waveform predictions with height of the ULVZ for event B.
(A) Observed Sdiff waveforms for event B. **(B-F)** Synthetic waveforms for ULVZs with a height of 10, 20, 30, 40, and 50 km. All waveforms filtered between periods of 30 and 50 s. The preferred model is 20 km in height.

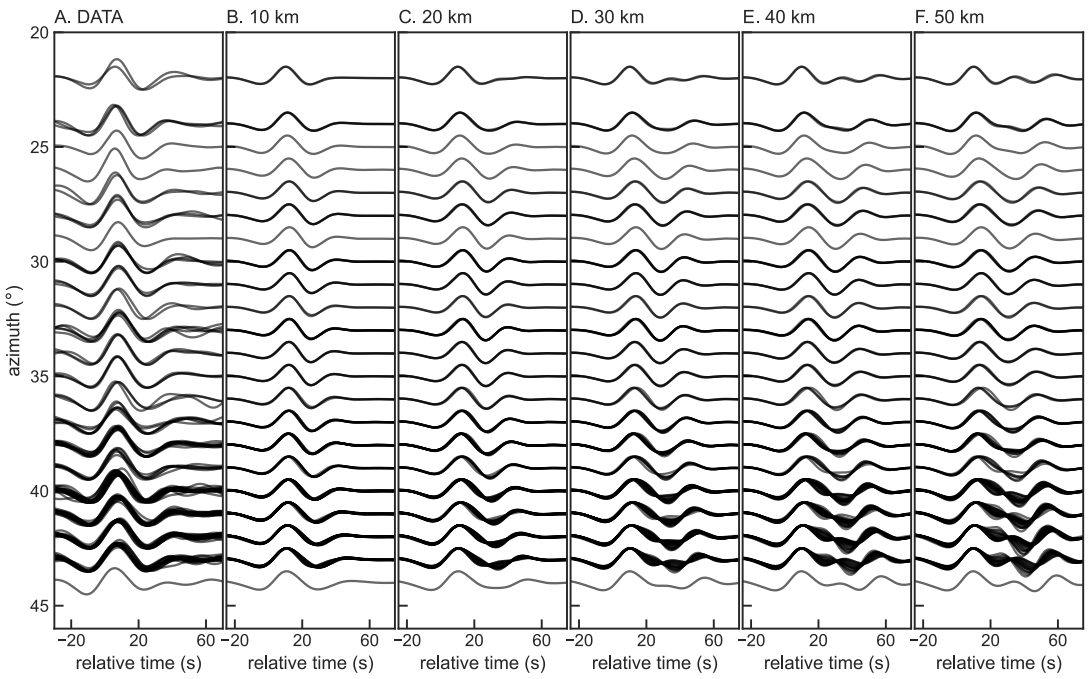

Fig. S12 Waveform predictions with height of the ULVZ for event C.
(A) Observed Sdiff waveforms for event C. **(B-F)** Synthetic waveforms for ULVZs with a height of 10, 20, 30, 40, and 50 km. All waveforms filtered between periods of 30 and 50 s. The preferred model is 20 km in height.

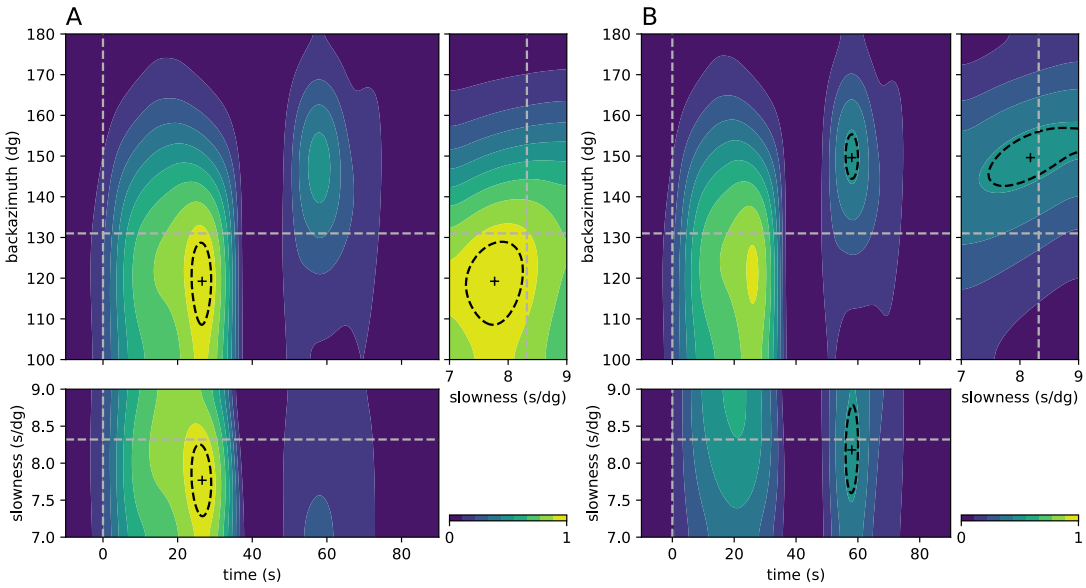

Fig. S13. Example of a normalized phase weighted envelope stack as a function of time, backazimuth, and slowness for a subset of 20 stations in Alaska for event A.
(A) Cross-sections are through the peak of the main Sdiff energy ($t = 27\text{s}, u_{hor} = 7.8\,{}^{\text{s}}/_{\circ}, \theta = 119°$). Black dashed lines show 95% contour around the peak used to pick the uncertainty. Grey dashed lines show reference time and slowness for an Sdiff wave in PREM (Dziewonski and Anderson, 1981), and the reference backazimuth from the center of the stack. **(B)** Same as (A), but for cross-section through the peak of the postcursor ($t = 58\text{ s}, u_{hor} = 8.2\,{}^{\text{s}}/_{\circ}, \theta = 150°$).

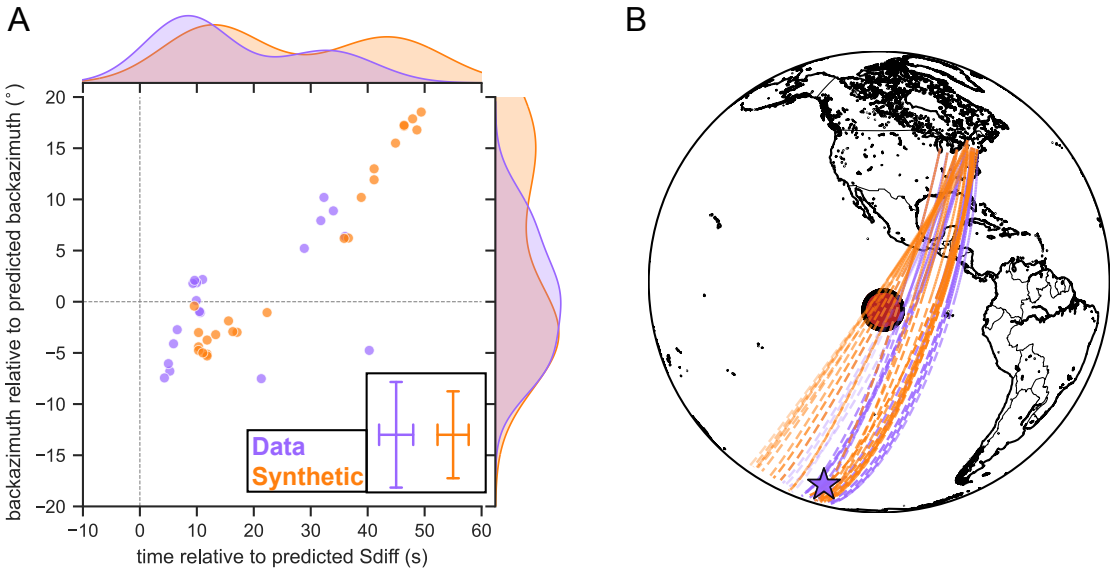

Fig. S14 Beamforming results for event C.
(A) Relative time vs. relative backazimuth for picked peaks in beamform stack for real data (purple) and synthetic data for the ULVZ model (orange). Error bars in lower right shows median uncertainty for the observations. **(B)** Back-projection of determined backazimuths for energy peaks. Projections are solid line up to 40° epicentral distance and dashed beyond up to 120° epicentral distance. Transparency reflects relative amplitude of the secondary postcursor peaks with respect to the main peaks.

Date	Dep [km]	Lat [°]	Lon [°]	Mw	Location
2021/08/14 - T	*26*	*55.21*	*-157.42*	*7.0*	*ALASKA PENINSULA*
2021/04/25	248	-21.70	-176.87	6.5	FIJI ISLANDS REGION
2021/04/24	315	-18.91	-176.13	6.6	FIJI ISLANDS REGION
2021/03/17	15	-41.40	-86.16	5.7	WEST CHILE RISE
2021/02/03	18	-36.38	-98.63	6.6	SOUTHEAST OF EASTER ISLAND
2020/11/03	*18*	*-44.61*	*-79.46*	*6.0*	*OFF COAST OF SOUTHERN CHILE*
2019/10/01	12	-56.13	-122.67	5.9	SOUTHERN EAST PACIFIC RISE
2019/09/29 - B	***17***	***-35.56***	***-73.10***	***6.7***	***OFF COAST OF CENTRAL CHILE***
2018/12/19	16	-36.17	-101.06	6.2	SOUTHEAST OF EASTER ISLAND
2018/11/30 - S	*48*	*61.49*	*-150.02*	*7.0*	*SOUTHERN ALASKA*
2017/07/04	12	-35.59	-73.56	5.9	OFF COAST OF CENTRAL CHILE
2017/02/24 - D	***418***	***-23.44***	***-178.77***	***7.0***	***SOUTH OF FIJI ISLANDS***
2016/12/25 - A	***22***	***-43.41***	***-73.94***	***7.6***	***SOUTHERN CHILE***
2016/08/18	13	-55.97	-123.63	6.0	SOUTHERN EAST PACIFIC RISE
2016/07/27	20	-44.62	-79.48	5.9	OFF COAST OF SOUTHERN CHILE
2016/01/24 - R	*111*	*59.75*	*-153.27*	*7.1*	*SOUTHERN ALASKA*
2015/06/20	12	-36.35	-74.10	6.4	OFF COAST OF CENTRAL CHILE
2015/05/19 - C	***15***	***-54.53***	***-132.39***	***6.6***	***PACIFIC-ANTARCTIC RIDGE***
2014/06/29	21	-55.34	-28.31	6.9	SOUTH SANDWICH ISLANDS REGION
2012/07/18	20	-55.36	-128.96	5.9	PACIFIC-ANTARCTIC RIDGE
2010/07/18	12	52.66	-169.64	6.7	FOX ISLANDS, ALEUTIAN ISLANDS
2010/05/20	12	-39.04	-92.33	5.9	SOUTHEAST OF EASTER ISLAND
2010/05/03	15	-38.31	-74.08	6.2	OFF COAST OF CENTRAL CHILE
2010/03/16	13	-36.49	-73.63	6.6	NEAR COAST OF CENTRAL CHILE
2010/03/05	15	-36.89	-73.75	6.6	NEAR COAST OF CENTRAL CHILE
2009/08/01	20	-55.70	-124.58	6.0	SOUTHERN EAST PACIFIC RISE
2008/11/22	*12*	*-37.15*	*-95.29*	*5.7*	*SOUTHEAST OF EASTER ISLAND*
2007/06/14	18	-36.22	-100.37	5.9	SOUTHEAST OF EASTER ISLAND
2007/05/07	20	-45.00	-81.21	6.0	OFF COAST OF SOUTHERN CHILE
2005/07/10	12	-36.38	-97.46	6.0	WEST CHILE RISE
2004/11/17	629	-19.87	-178.40	6.5	FIJI ISLANDS REGION
2004/07/15	577	-17.68	-178.52	7.0	FIJI ISLANDS REGION
2004/01/25	143	-16.75	-173.79	6.6	TONGA ISLANDS
2002/07/19	15	-57.07	-140.94	6.0	PACIFIC-ANTARCTIC RIDGE
1995/09/08	15	-56.15	-122.69	6.3	SOUTHERN EAST PACIFIC RISE

Table S1.

Earthquake event dates and parameters showing postcursor evidence in their ScS/Sdiff waves crossing the Galápagos ULVZ. Events in ***bold+italic*** are used in the main paper and A-D labels are included. Events in *italic* are shown in the supplements and R-T labels for events in Figures S3 and S4 are included. All earthquake parameters are for the Global Centroid-Moment Tensor project (www.globalcmt.org, (Ekström, Nettles and Dziewoński, 2012)) except for

2016/12/25-A, for which we use the W-phase solution published by the USGS National Earthquake Information Centre.

Movie S1.
Animation of interaction between the wavefront and the ultra-low velocity zone for Event A using a modified version of the wavefront tracker by (Hauser, Sambridge and Rawlinson, 2008). Only horizontal propagation is considered. Event location - blue star, seismometer locations – blue triangles. Velocities show the shear wave velocity deviations at 2800 km depth from the tomographic SEMUCB-WM1 (French and Romanowicz, 2014) and the ultra-low velocity zone.

Movie S2.
Animation of interaction between the wavefront and the ultra-low velocity zone for Event B using a modified version of the wavefront tracker by (Hauser, Sambridge and Rawlinson, 2008). Only horizontal propagation is considered. Event location - blue star, seismometer locations – blue triangles. Velocities show the shear wave velocity deviations at 2800 km depth from the tomographic SEMUCB-WM1 (French and Romanowicz, 2014) and the ultra-low velocity zone.

Movie S3.
Animation of interaction between the wavefront and the ultra-low velocity zone for Event C using a modified version of the wavefront tracker by (Hauser, Sambridge and Rawlinson, 2008). Only horizontal propagation is considered. Event location - blue star, seismometer locations – blue triangles. Velocities show the shear wave velocity deviations at 2800 km depth from the tomographic SEMUCB-WM1 (French and Romanowicz, 2014) and the ultra-low velocity zone.

Movie S4.
Animation of interaction between the wavefront and the ultra-low velocity zone for Event D using a modified version of the wavefront tracker by (Hauser, Sambridge and Rawlinson, 2008). Only horizontal propagation is considered. Event location - blue star, seismometer locations – blue triangles. Velocities show the shear wave velocity deviations at 2800 km depth from the tomographic SEMUCB-WM1 (French and Romanowicz, 2014) and the ultra-low velocity zone.